

Design of π -conjugated flexible semiconductive 2D MOF and MOF derived CuO nano-spheres for solvent free C-X (S, O) hetero-coupling catalysis with enhanced conductivity

Maxcimilan Patra^{a,1}, Soumen Kumar Dubey^{a,1}, Bibhas Mondal^a, Kajal Gupta^a, Angshuman Ghosh^b, Subhankar Mandal^c, Satyajit Hazra^c, Ajit Kumar Meikap^{d,*}, Ujjal Kanti Roy^{a,*}, Subham Bhattacharjee^{a,*}, Rajat Saha^{a,*}

^a Department of Chemistry, Kazi Nazrul University, Asansol-713340, India

^b TCG Lifescience, Block BN, Sector V, Saltlake, Kolkata-700156, India

^c Saha Institute of Nuclear Physics, HBNI, 1/AF Bidhannagar, Kolkata 700064, India

^d Department of Physics, NIT Durgapur, Durgapur-713209, India

ARTICLE INFO

Article history:

Received 1 January 2021

Received in revised form 15 April 2021

Accepted 28 April 2021

Keywords:

2D MOF

$\pi \cdots \pi$ Interaction

Flexible MOF

MOF derived CuO-NPs

Green catalysis

Electrical conductivity

ABSTRACT

A flexible, 2-fold interpenetrated 3D supramolecular structure $[\text{Cu}(\text{ndc}^{2-})(1,10\text{-phen})]_n$ (where $\text{ndc}^{2-} = 2,6\text{-naphthalenedicarboxylate}$ and $1,10\text{-phen} = 1,10\text{-phenanthroline}$) comprising neutral 2D metal-organic layers as the basic building block was prepared. Structural study reveals that metal ions are bridged by ndc^{2-} ligands to form 2D coordination layers and the coordinated 1,10-phen moieties are hanging from the layers in the interlamellar spaces. The gliding motion of $\pi \cdots \pi$ stacked layers through 1,10-phen moieties was found to be responsible for the flexibility of MOF and the consequent extended conjugation also rendered semiconducting behaviour in the material. Thermal stability studies revealed that the framework was pretty stable below 260°C. Additionally, the MOF was characterized by performing BET adsorption and photoluminescence studies. Further, the MOF was calcinated at 650°C to prepare well defined, nearly uniform and spherical shaped CuO nanoparticles (CuO-NPs) with an average size of ~ 25 nm. Interestingly, CuO-NPs showed around 16 times more conductivity (4.8×10^{-2} S/cm) in relative to the parent MOF (3×10^{-3} S/cm). CuO-NPs induced cross-coupling reactions of alcohols and thiols with arylhalides have been reported. A simple, general, ligand-free and solvent-free procedure for the efficient synthesis of the cross-coupled products in high yield was successfully demonstrated.

© 2021 Elsevier B.V. All rights reserved.

1. Introduction

In last three decades, metal-organic frameworks (MOFs) are appeared as one of the most promising functional material due to their inherent porous structure and modular behaviour [1]. Initially, the inception was that the implication of inert metal ions and insulating bridging ligands makes MOFs weakly conducting or insulating in nature [2]. But, from last decade, design of conducting MOFs has gained much attention due to their several applications in energy storage, sensing, electrocatalysis, etc. [3]. Researchers have developed two different types of conductive MOFs: (a) intrinsically conductive MOFs: electrically conducting

organic building blocks, such as 2,3-pyrazinedithiolate [4], dihydroxybenzoquinone [5] etc. have been used to induce conductivity in the designed framework, and (b) extrinsically conductive MOFs: electrically conducting guests, both neutral I_2 , [6] (TCNQ) [7], and charged (BF_4^-) [8], are incorporated in the void space of MOFs to enhance conductivity. Intrinsically conducting MOFs have gained much attention over its extrinsic counterpart due to low cost production and easy synthesis [2a], [9]. Several types of design principles have been adopted by scientists to build intrinsically conducting MOFs: (a) use of metal ions and bridging ligands having equivalent band structure which will help to transport electrons through the framework [10], (b) use of radical generating ligands that will boost the conductivity of the designed framework [5c,10b] (c), use of extended $\pi \cdots \pi$ conjugation between 2D coordination polymer [5b], [11]. In organic electronics, π -interaction is used to develop conducting materials [12] and, in similar way, several research groups have developed conducting MOFs based on extended $\pi \cdots \pi$ conjugation using different

* Corresponding authors.

E-mail addresses: meikapn1td@yahoo.com (A.K. Meikap), uroccu@gmail.com (U.K. Roy), sbpb2012@gmail.com (S. Bhattacharjee), rajat.saha@knu.ac.in (R. Saha).

¹ Both have equal contributions.

organic ligands e.g. naphthalenediimide, [9b] tetrathiofulvalene [13], anthracene [14], etc. Formation of continuous π -conjugation throughout the framework is the primary condition to design such materials. Herein, we have used 1,10-phen, highly potential to participate in $\pi \dots \pi$ interaction, as the building block to develop conducting material and found that the synthesized 3D supramolecular framework showed semiconducting behaviour.

Recently, syntheses of various nano-materials using MOFs as sacrificial scaffolds are of great interest [15]. The regular periodic arrangement of metal nodes within the MOF architecture provides an excellent platform to design nano-particles of uniform size distribution as well as their intriguing porosity. The structure, composition, phase and size of the nano-particles can be controlled by optimizing the synthetic conditions: chemical environment (O_2 , N_2 etc.), temperature and synthetic methods [16]. Several research groups have synthesized metal, [16a] metal-oxide, [16b,16c,16d,16e,16f,16g] mixed metal-oxide, [16h] metal carbide [16i] NPs, etc. and explored their enormous applications in gas adsorption, [16j] catalysis, [16b] and so on. Besides, these MOF derived NPs have been used for several types of electronic applications like electrocatalysis, [17] battery, [18] etc. based on their versatile conducting properties from insulating to metallic behaviour [17–19]. In this work, we have used our synthesized semiconductive MOF to develop NPs and interestingly found that the MOF-derived NPs showed higher conductivity than the parent MOF.

C–O and C–S bonds are prevalent in numerous compounds that are of biological, pharmaceutical, and material interest [20]. Specially, a large variety of aryl sulfides are in use for diverse clinical applications [21]. One of the most common synthetic methods for their preparation is the copper-assisted classic Ullmann reaction. However, these reactions often require harsh conditions such as high temperature ($>200^\circ C$), stoichiometrically higher amount of copper reagent and thus produce a lot of wastes [22]. Currently, to follow strict environmental laws, chemical based industries are desperate in reducing various harmful chemical wastes by designing intelligent catalysts those perform in mild or environment benign conditions with high yield, large selectivity and good efficacy [23]. Palladium and copper complexes containing electron-rich ligands have been studied considerably for the cross-couplings of oxygen and sulphur nucleophiles with aryl halides [24]. Subsequently, few studies have focused on the use of iron and nickel-based catalytic systems for this purpose also [25]. Unlike homogeneous catalyst, use of heterogeneous catalyst is much more advantageous in terms of their easy separation, recyclability, high thermal stability and longer lifetime. In this respect, we have focused on CuO-NPs induced heterogeneous C(aryl)-S and C(aryl)-O hetero-coupling reactions with the following advantages: (a) the reaction proceeds under solvent free condition, (b) easy separation of catalysts and products from the reaction mixture after completion, (c) high selectivity of the catalysts for the substrate, (d) high catalysis rate and e) re-usability.

In this endeavour, we have synthesized a 2-fold interpenetrated, flexible, 3D supramolecular framework: **[Cu(2,6-ndc)(1,10-phen)]_n**, by solvothermal method and characterized by SCXRD analysis. Structural analysis revealed that each Cu centres are connected by 2,6-ndc ligands to form 2D coordination layers with hanging coordinated 1,10-phen moieties and these 2D metal-organic coordination layers are assembled by 1,10-phen mediated $\pi \dots \pi$ interactions to form the overall 3D supramolecular structure. The presence of $\pi \dots \pi$ interactions help to: (i) induce flexibility and (ii) create electronic conducting pathway within the framework. The resultant flexible framework showed semiconducting nature in association with micro-porosity. TGA analysis revealed that the framework decomposes at $350^\circ C$. The MOF was decomposed by heating at $650^\circ C$ to produce CuO-NPs

which were characterized by PXRD, SEM and EDAX analyses. Four probe electrical conductivity experiments revealed that the synthesized CuO-NPs have 16 times higher conductivity than parent MOF. Further, we have successfully demonstrated solvent free C–S and C–O heterocouplings in excellent yields in bulk utilizing the CuO-NPs. Product analysis revealed exclusive formation of the desired products with minimum amounts of wastes; hence, we would be able to make the process green and highly applicable for industrial scale synthesis.

2. Experimental section

Materials and Methods: Copper (II) nitrate, monohydrate; 2,6-naphthalene dicarboxylic acid and 1,10-phenanthroline were purchased from Merck chemical company. All other chemicals used were AR grade. Elemental analysis (C, H, N) was carried out using a Perkin-Elmer 240C elemental analyzer. The thermal analysis was carried out using a Mettler Toledo TG-DTA 85 thermal analyzer under a flow of N_2 (30 ml/min). The sample was heated at a rate of $10^\circ C/min$ with inert alumina as a reference. IR spectroscopy was measured on Nicolet Impact 410 spectrometer between 400 and 4000 cm^{-1} , using the KBr pellet method. Photoluminescence spectra were collected on a Shimadzu RF-5301PC spectrofluorometer. Powder XRD patterns were recorded by using Cu-K α radiation (Bruker D8; 40 kV, 40 mA). The elemental analysis for CuO-NPs was performed by BRUKER energy dispersive X-ray spectrometer (EDS) attached with the FEI, INSPECT F50 field emission scanning electron microscope (FESEM). 1H -NMR studies were carried out by using 300 MHz Bruker NMR spectrometer. The XPS measurements of the sample was carried out in an ultrahigh vacuum (UHV) multiprobe setup (Omicron Nanotechnology) at a base pressure of $\sim 2.0 \times 10^{-9}$ mbar, which was equipped with an EA125 hemispherical energy analyzer and an X-ray source [26]. For the XPS measurements, monochromatic Al K α X-ray of 1486.6 eV photon energy was used as a source and the corresponding spectrometer energy resolution was ~ 0.8 eV. C 1s level (binding energy of 284.8 eV) was chosen as the reference level to calibrate the other core-level spectra.

Synthesis of Complex 1 **[Cu(O-phen)(ndc)]_n**: A mixture of $Cu(NO_3)_2$ (0.5 mmol, 0.1214 g), ndc (0.5 mmol, 0.1092 g), 1,10-phen (0.25 mmol, 0.0502 g) and 1 mL Et_3N in 6 mL DMF was stirred for 15 min. Then the mixture was transferred into a 15 ml Teflon-lined stainless-steel vessel and heated for 24 h at $120^\circ C$. Afterwards, it was cooled to room temperature for another 24 h. After 48 h, green coloured single crystals (Figure S1) suitable for X-ray structure determination were isolated by filtration. Yield: 70%. Anal. Calcd. for $C_{24}H_{14}CuN_2O_4$ indicates C: 62.85% (62.88% theo), H: 3.10% (3.12% theo) and N: 6.10 (6.08% theo). IR (KBr pellet, cm^{-1}): 1606(s), 1560(s), 1544(w), 1426(w), 1394(s), 1357(s), 1221(w) and 1191(w) (Figure S2).

Electrical conductivity measurement: The resistance of the sample is measured by means of a four terminal direct current technique with resolution of $\delta R/R = 10^{-5}$ using a pressed pellet (10 ton pressure) of the samples. The four terminal connections are made using fine copper wire with pure silver paste. As a confirmatory test towards ensuring good electrical contact using silver paste, the continuity of the samples was checked before placing it within the sample holder. Contribution of conductivity of silver of the paste is ignored as it is used for all cases. All these measurements were performed by the following equipments, (i) A constant current source (KEITHLEY INSTRUMENT, Model 220), (ii) A nanovoltmeter (KEITHLEY INSTRUMENT, Model 181), (iii) Hewlett Packard 3458 A, 81/2 digit multi-metre.

General Procedure for C-X (X = S and O) Hetero-coupling Reactions: The catalytic reactions were carried out in a glass batch reactor. To a stirred solution of the phenol or thiophenol

(25 mmol), aryl halide (5 mmol), KOH (5 mmol) and CuO (2.5 mol%) were added, and the reaction mixture was stirred at 100 °C for 17 h under inert atmosphere and monitored continuously by TLC (hexane/ethyl acetate = 9:1 v/v). After completion of the C–O or C–S cross-coupling of phenol/thiophenol with aryl halide, (i.e. after complete consumption of the aryl iodide which takes near about 17 h), the reaction mixture was treated with diethyl ether. The solution was centrifuged and then catalyst was isolated, washed with water and ether. After complete drying, the catalyst can be reused for the next cycle. The remaining mixture was diluted with water and extracted with diethyl ether thrice. The combined organic layer was dried over anhydrous Na₂SO₄, filtered, and concentrated to afford the crude material. The crude material was then purified by column chromatography (silica 100–200 mesh, ethyl acetate-hexane 5%–10%) to afford the desired C–O or C–S cross coupling product (yield = 95%–99%).

Crystallographic Data Collection and Refinement: Suitable single crystal of the complex was mounted on a Bruker SMART diffractometer equipped with a graphite monochromator and Mo-K α ($\lambda = 0.71073 \text{ \AA}$) radiation. Unit cell parameters were determined by using the APEX2 [27] program. Data reduction was carried out by the SAINT [27] program and correction or absorption was performed using the SADABS [27] program. The structure was solved using Patterson method by using the SHELXS-2018/3 [28] embedded in WINGX software package [29]. Subsequent difference Fourier synthesis and least-square refinement revealed the positions of the remaining non hydrogen atoms. Non-hydrogen atoms were refined with independent anisotropic displacement parameters. Hydrogen atoms were placed in idealized positions and their displacement parameters were fixed to be 1.2 times larger than those of the attached non-hydrogen atom. All Figures were drawn by using PLATON [30] and ORTEP [31]. Data collection and structure refinement parameters and crystallographic data for complex 1 are given in Table S1. The structure was previously reported in literature [32] and, herein, we have described from a different perspective. Some selected coordination bond lengths, bond angles and non-covalent interaction parameters are summarized in Table S2–S3.

Indexing of the PXRD data: The indexing of the XRPD pattern was carried out using NTREOR and McMaille programs of EXPO 2009. Indexing reveals that the complex is still crystalline with a monoclinic system with $a = 13.5426 \text{ \AA}$, $b = 13.9326 \text{ \AA}$, $c = 12.0862 \text{ \AA}$, $\beta = 100.1023^\circ$ and $V = 2245.11 \text{ \AA}^3$. The space group was obtained from statistical analysis of the powder pattern with the help of find space module of the EXPO 2009 software package. Statistical analysis shows that the most probable space group is P2₁/n. For this unit cell and space group, full pattern decompositions were performed using Le Bail method giving good fit between calculated and experimental powder X-ray patterns. This result was corroborated from the indexing and Pawley refinement of the PXRD pattern of the complex by the reflex module of the Material studio program. Unit cell, peak profiles, zero-shift, background were refined simultaneously. Peak profiles were refined by the Pseudo-Voigt function with Berar-Baldinozzi asymmetry correction parameters. The background was refined using a 4th order polynomial.

3. Result and discussions

Structural description of Complex 1: X-ray crystal structure analysis revealed **1** as a neutral 3D supramolecular framework (formula [C₂₄H₁₄CuN₂O₄]_n). The asymmetric unit contains one Cu(II) ion, two halves two ndc²⁻ ligands and one 1,10-phen (Figure S3). Each Cu(II) atom shows distorted square pyramidal geometry ($\tau = 0.07$) with CuN₂O₃ chromophore (Figure S4).

ndc²⁻ ligands show two different types of bridging modes: μ -4-bis-bridging and μ -2-bis-bridging. Coordination of two different types of ndc²⁻ with the Cu²⁺ ions forms 2D coordination sheet in the **bc**-plane with 1,10-phen ligands hanging into the interlamellar spaces from the metal centres, Figure S5. These 1,10-phen moieties between two 2D layers are connected through are interacted by $\pi \dots \pi$ interactions between aromatic rings present within the 1,10-phen molecules. Such $\pi \dots \pi$ interactions further assemble these 2D layers along *a*-axis to generate a spongy 3D supramolecular framework, as shown in Fig. 1a. The dimensions of all $\pi \dots \pi$ interactions are listed in Table S4. It is to be noted that 1D channel of dimension $12.071 \times 13.294 \text{ \AA}$ is formed along *a*-axis (Figure S6). The channel is filled by two-fold self impregnation in order to achieve an efficient packing (Fig. 1b and S7).

Framework Stability and PXRD: Thermo-gravimetric analysis of the compound was performed in the temperature range of 25–500 °C under N₂ atmosphere (Fig. 2). The TG analysis indicated that complex **1** is stable up to 260 °C and undergoes decomposition in two consecutive steps above this temperature. In the first step, 1,10-phen moieties undergo dissociation within 260 and 300 °C and above this temperature it degrades in another step at about ~325 °C.

To know about framework flexibility, the PXRD analyses with complex **1** were done at room temperature and at 150 °C temperature. The PXRD pattern of the as synthesized complex **1** is matched very well with the simulated pattern which indicated the phase purity of the sample. The PXRD (Fig. 3) pattern at higher temperature has peaks at slightly lower angle. The indexing of the PXRD pattern was carried out using NTREOR and McMaille programs of EXPO 2009 (supporting information, Figure S8). This reveals that the complex is still crystalline with monoclinic system ($a = 13.5426$, $b = 13.9326$, $c = 12.0862 \text{ \AA}$, $\beta = 100.1073^\circ$ with a larger cell volume of 2245.11 \AA^3 , Table S4). So, the length of the *a*-axis, along which 2D layers are stacked through $\pi \dots \pi$ interactions, increases in large amount compared to *b*- and *c*-axes and this corresponds to the expansion of layer gap assisted by the gliding motion of the π -stacked layers [33], which is feasible for 1,10-phen ligand. So, both the increase in bond length and expansion of layer gap along *a*-axis contribute to the overall 15% increase in the overall cell volume. Upon cooling to room temperature, the PXRD pattern reverts back to the original pattern. This proves the π -induced flexibility of the framework.

Adsorption study: Though PLATON study indicates the non-porous nature the framework at ambient condition but the variable temperature PXRD study showed that there is a chance to create porous channel along crystallographic *c*-axis by thermally stimulated π -induced flexibility – and thus we have attempted to analyse sorption behaviour of the sample. N₂ adsorption study at 77 K revealed the non-porosity of the material while the solvent sorption studies at 298 K indicated micro-porosity. Water adsorption isotherm (at 298 K) of complex showed type III behaviour. The volume uptake of water is $15.6 \text{ cm}^3/\text{g}$ (Fig. 4). Complex **1** also adsorbs $12.9 \text{ cm}^3/\text{g}$ methanol and $6.24 \text{ cm}^3/\text{g}$ ethanol (Fig. 4). Small amount of adsorption may be interpreted as that due to interpenetration very narrow channels were created within the framework or surface adsorption [34]. Desorption curve does not coincide with the adsorption curve in all cases, showing a hysteresis loop and incomplete desorption. A very little amount of water, methanol and ethanol remains within the framework. Small hysteresis in the water adsorption isotherm is probably because of trapping by the coordinatively unsaturated metal sites.

Photoluminescence: Photoluminescence property of complex **1** was performed at room temperature in solid state. The emission spectra of both 1,10-phen ligand and complex **1** are shown in

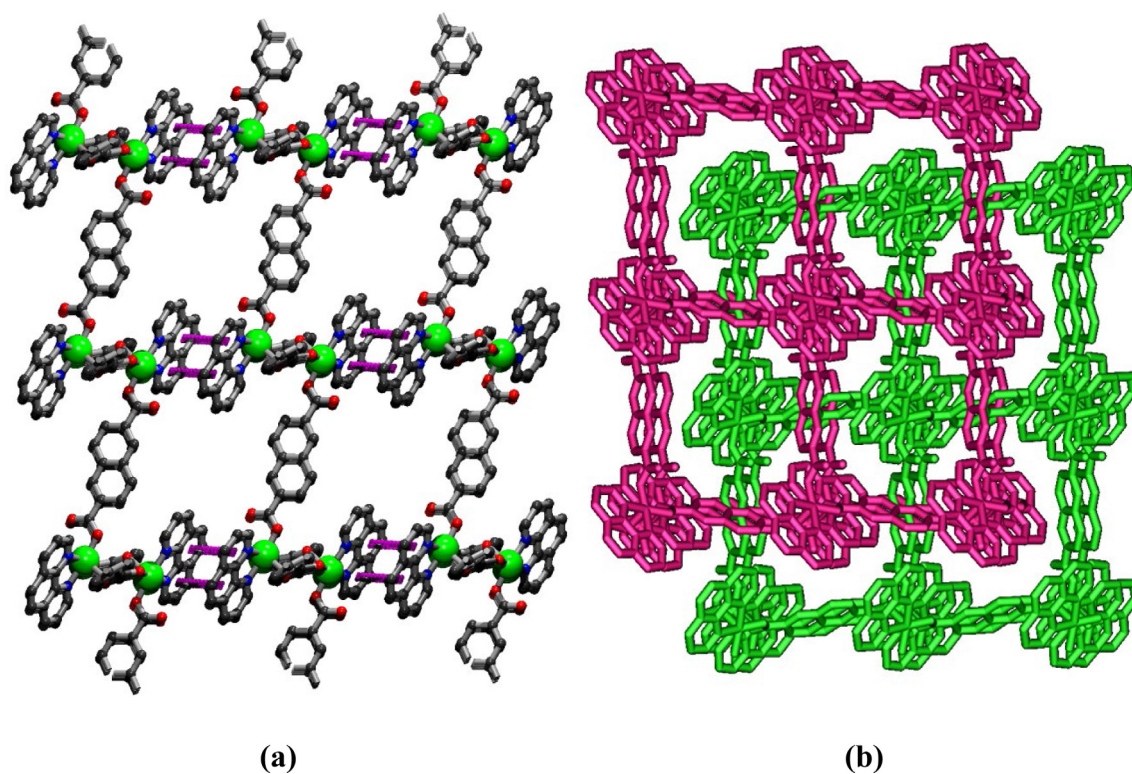


Fig. 1. $\pi \dots \pi$ (magenta) conjugated 3D supramolecular structure (a) and 2-fold interpenetration (b) of complex **1**. (For interpretation of the references to colour in this figure legend, the reader is referred to the web version of this article.)

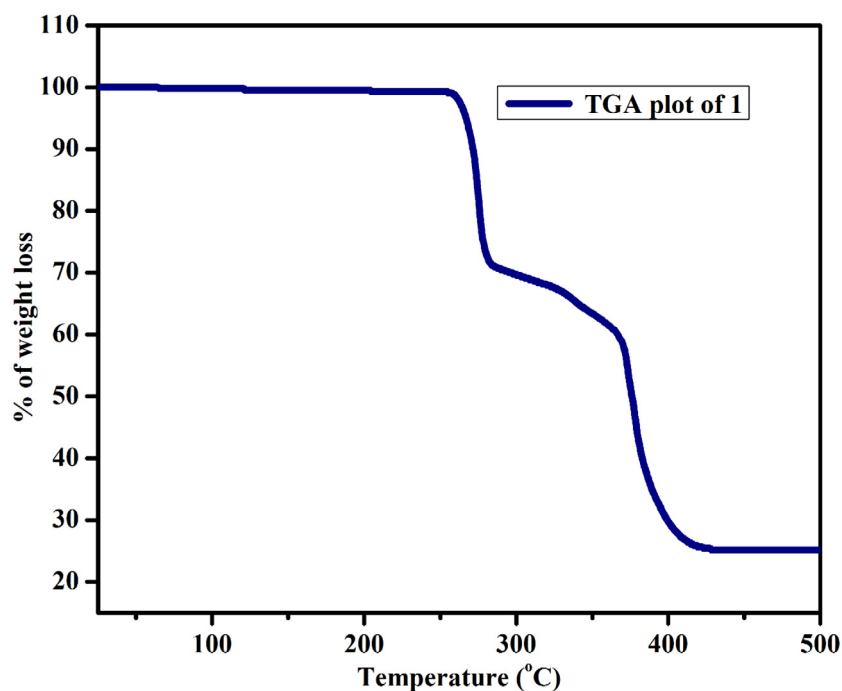


Fig. 2. The thermal plot of complex **1**.

Figure S9. The luminescence spectra of 1,10-phen ligand show two peaks at 412 nm and 434 nm with a shoulder at 461 nm. The spectra arise due to $\pi-\pi^*$ transition. The luminescence spectra of complex **1** show similar pattern – the spectra contain two peaks at 414 nm and 434 nm with three different shoulders at 458 nm,

464 nm and 468 nm. The spectra arise due to both intra-ligand $\pi-\pi^*$ transition and M-L charge transfer transition. So due to metal complex formation, a small red shift occurs.

Synthesis and Characterization of CuO-NPs: Nano-particles are highly interesting as their properties are critically dependent on synthetic condition, size distribution, morphology and shape.

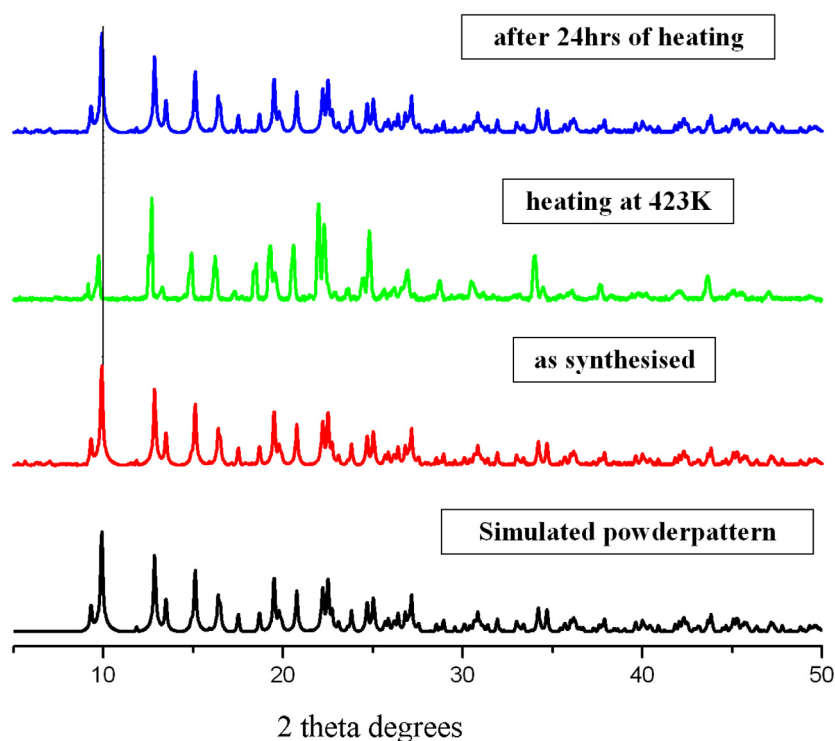


Fig. 3. Variable temperature PXRD pattern of **complex 1**.

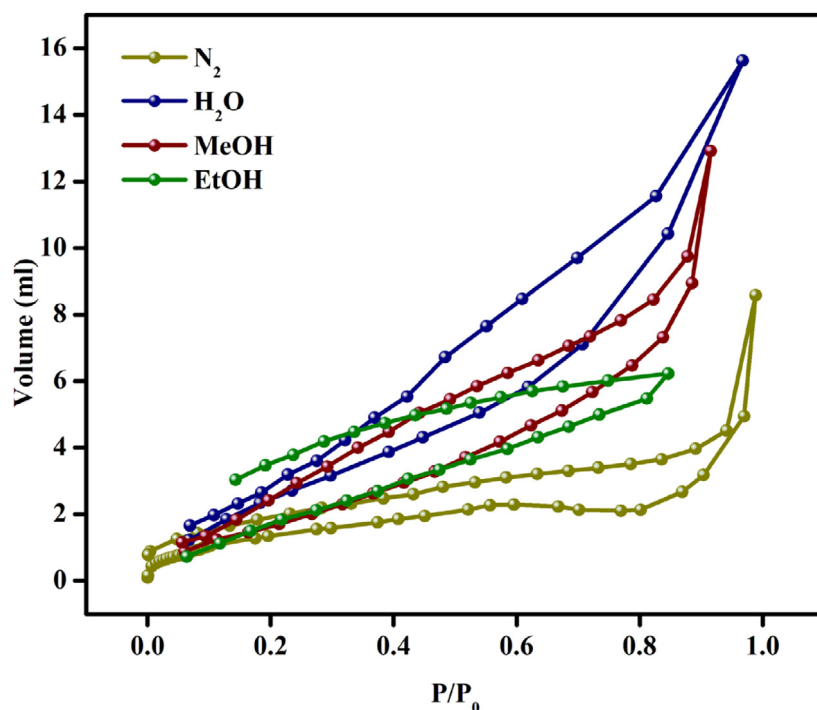
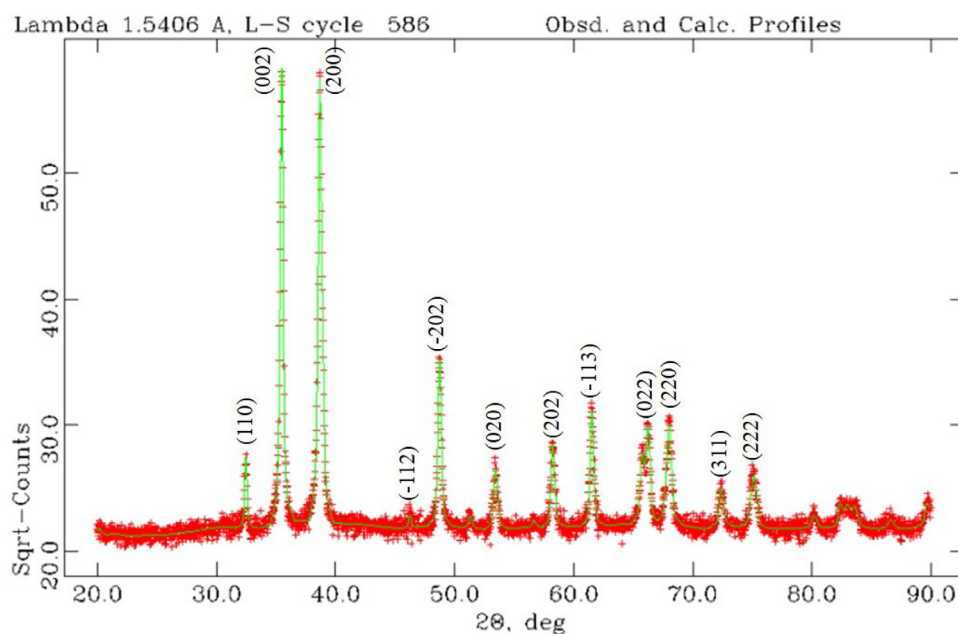


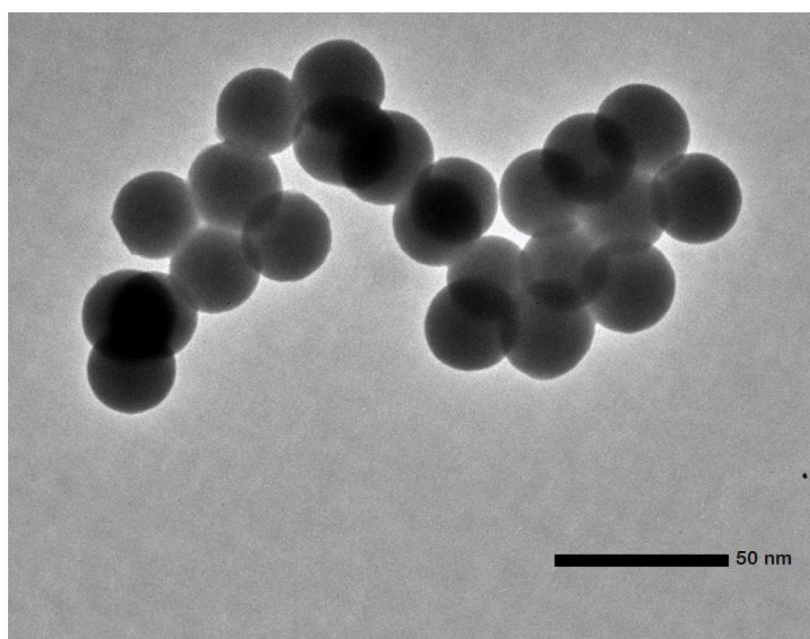
Fig. 4. Gas and solvent sorption behaviour of **complex 1**.

CuO-NPs have great potential for their applications in electrochemical cells, magnetic storage media, photovoltaic cells, etc. Here, the 2D-MOF is used as a template to synthesize CuO-NPs by calcinations. The bulk material of the MOF was heated at 650 °C for 4 h at normal condition. Upon heating, the green coloured compound turned in black powder, which was characterized by PXRD, EDS, IR, TEM and SEM analyses. IR spectra of the CuO-Nps are presented in Figure S10. The PXRD pattern matches

with the reported PXRD pattern of CuO with JCPDS No. 08-0234 (Fig. 5a). The TEM micrograph indicated the spherical morphology of the synthesized NPs (Fig. 5b) with average size of ~25 nm and this corroborates with the PXRD data. EDS study indicated the presence of characteristic peaks for the constituents (Cu and O) (Figure S11). The Cu 2p_{3/2} core-level spectra (Fig. 6) have been studied to know the oxidation state of Cu present in the copper oxide nanoparticles. The binding energy position of the



(a)



(b)

Fig. 5. PXRD pattern (a) and TEM image (b) of the synthesized CuO-NPs.

main peak in the spectra was observed at around 933.7 eV that informs about the presence of Cu^{2+} species, which was observed previously by many people [35]. The strong shake-up satellite observed in these spectra is also an indication of the presence of Cu^{2+} species that was mentioned by many authors previously [35]. So, the Cu $2p_{3/2}$ core-level spectra confirm that the Cu present in this copper nanoparticles sample is mostly in the Cu^{2+} oxidation state.

Green Catalytic C-X Hetero-coupling Reactions: In the present work, the synthesized spherical shaped CuO-NPs are used for the catalytic cross-coupling (C-O and C-S) reactions of alcohols

and thiols with arylhalides. Generally, for such C-O and C-S cross-coupling reactions, high boiling solvents like DMSO, DMF, NMP, etc. are required in both homogeneous and heterogeneous conditions. And consequently, separation of products from these solvents becomes very difficult and tedious. Here, we are going to report a solvent free, neat reaction protocol for such hetero-coupling reactions of phenol, thiophenol, alcohol, and thiols with aryl halides.

Literature review indicates that in previous studies of copper-catalyzed hetero-coupling reactions, *N*-methylpyrrolidinone (NMP), dimethylformamide (DMF), dimethylsulfoxide (DMSO)

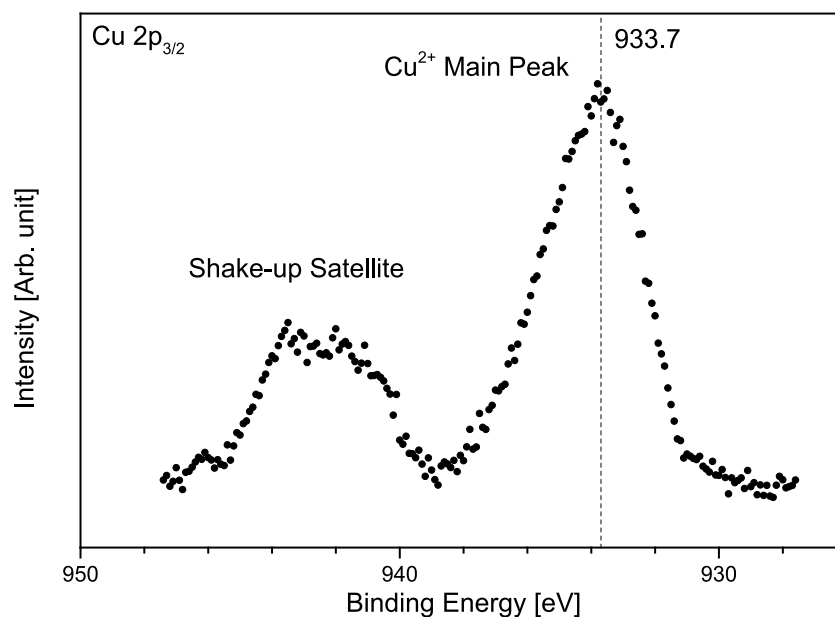


Fig. 6. XPS data of CuO-NPs reveals the presence of only Cu^{2+} ions.

etc. are used as solvent with KOH and K_2CO_3 as base [36] and, thus here, we have also followed the same protocol initially. Punniyamurthi et al. have carried out the C-X (X = S, N and O) hetero-coupling catalytic reactions using CuO-NPs in DMSO [36d]. Here, catalytic activity of the synthesized CuO-NPs was first investigated for the cross-coupling of iodobenzene with phenol and latter with thiophenol. The reactions of chlorobenzene, bromobenzene, phenyltosylate, and phenylboronic acid are studied, but those are found to be inferior to that of aryl iodides. Catalytic tests were also performed with CuCl, CuBr and CuI, freshly prepared before use, provided the same results as obtained with synthesized CuO-NPs. Other Cu(II) salts tested (CuBr_2 , $\text{CuSO}_4 \cdot 5\text{H}_2\text{O}$, CuCl_2) were found to be less efficient catalysts (yields 55%–69%) than the CuO-NPs. A low amount of 2.5 mol % of CuO-NPs was employed in these initial standardization reactions. Our first goal was to optimize reaction conditions and to achieve information about the role of additives and solvent polarity. It appeared that, by applying KOH as base in DMF, diphenylether was obtained in quantitative yield in presence of 20 mol% CuO-NPs catalyst without the use of added ligands. Solvent polarity has significant impact on the yield of the reactions (Table S5) – high polarity solvents like DMF, DMA and NMP show better yield than toluene (entries 3–5). It is noteworthy that very low yield (40%) was obtained for using water as solvent (Table S5, entry 6). Now, difficulty in separation of these solvents from the product prompted us to choose the neat reaction conditions (Table S5, entry 7). And interestingly, we have found that the yield of neat reaction conditions are similar to that in DMF, DMA and NMP and then we decided to go further with the neat reaction conditions.

Similarly, a series of bases were also screened. Among inorganic bases, KOH gave almost quantitative results for the coupling reaction to diphenylethers (Table S6), while, among organic bases, triethylamine and Hunig's base (DIPEA) gave also good results (Table S6, entries 2 and 3) in heterogeneous reaction mixture. Notably, in our case the required amount for the base is only one equiv. (based on the aryl halide), while in common reports this is usually in between 1.5 and 2.5 equiv. Further experiments were performed to find the optimal reaction temperature and reaction time. Both Tables S5 and S6 refer to around 17 h reaction with temperature of 100 °C. It was noted that a small decrease in temperature of only 10 °C caused a significant decrease in

Table 1

Reaction of Aryl Iodides with Phenol and Thiophenol (conditions: phenol or thiophenol (25 mmol), aryl iodide (5 mmol), KOH (5 mmol), CuO (2.5 mol%), 100 °C, 17 h.

Entry	Aryl iodide	Alcohol or thiol	Product	Yield (%)
1	PhI	PhOH	Ph-O-Ph	99
2	PhI	PhSH	Ph-S-Ph	99
3	PhI	PhCH ₂ OH	PhCH ₂ -O-Ph	95
4	PhI	PhCH ₂ SH	PhCH ₂ -S-Ph	95

diaryl thioether yield (85%). Lowering the time of the reaction in the present conditions also decreases the yield of the desired products. Accordingly, at 100 °C, the reaction of iodobenzene with phenol is relatively fast (65 and 95% after 2 and 6 h, respectively). It also appeared that fluoro-, chloro-, and bromobenzene are very less reactive under the optimized conditions, giving extremely lower yields (4%–55%) of the C–O coupling products (Table S7). Aryltosylate and boronic acids are also very less effective compared to that of iodide (Table S7, entries 5 & 6). Finally, the effect of the copper catalyst and its loading amount was evaluated. As discussed earlier and shown in Table S8, Cu(II) catalysts performed badly (Table S8, entries 1–4, yields 55%–69%). Only a minor difference in yields were observed when catalytic activity of CuO-NPs was compared with Cu(I) salts (Table S8, entries 5–8). The desired products are purified by column chromatography, identified by NMR spectra and then the isolated yield was calculated.

To determine the scope of the catalytic system, the present protocol was further applied to reactions of a variety of commercially available aryl iodides and phenols or thiophenols (Table 1). As shown in Table 1, the coupling of phenol and thiophenol with iodobenzene was successful, leading to the desired products in good yields. The protocol is equally efficient for aromatic and aliphatic phenols and thiophenols. The catalyst system is highly efficient providing the corresponding diaryl ethers and thioethers in good to excellent yields. Iodobenzene was maintained as arylating substrate. The present optimized catalytic process provides the arylation of phenols and thiophenols with aryl iodides, in the presence of KOH as a base under neat conditions. To the best of our knowledge, this is the first report about aryl-sulphur and aryl-oxygen bond formation in which a MOF derived CuO-NPs catalyst

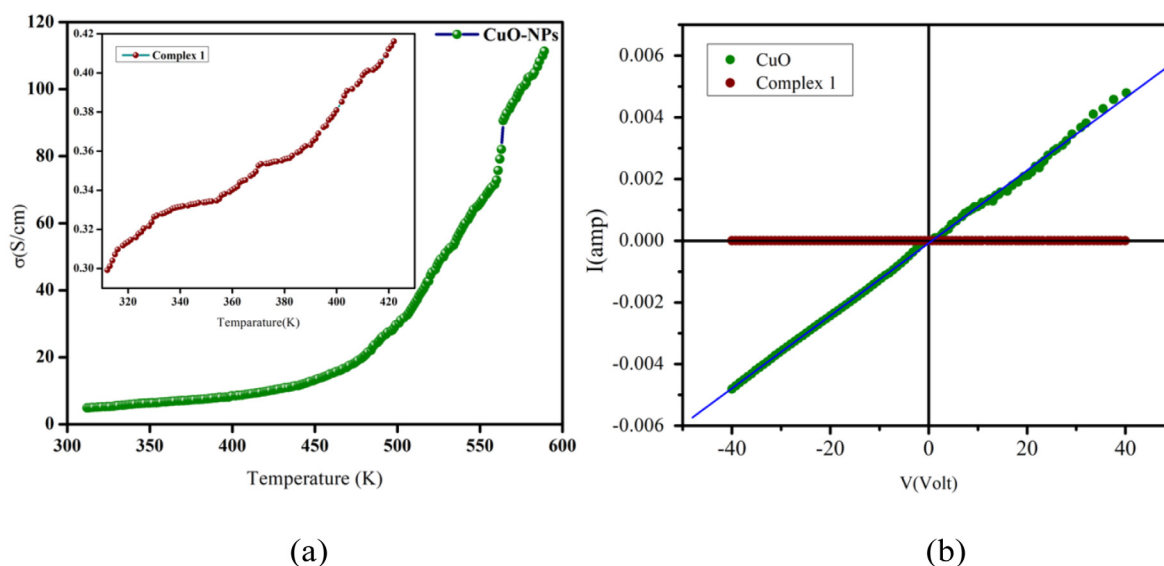


Fig. 7. Variable temperature electrical conductivity and corresponding I-V curve of the both complex **1** and MOF derived NPs.

is used without addition of any ligand and solvent. In the present study diphenylether and diphenylthioether was formed in 99% yield in the reaction of iodobenzene with phenol and thiophenol in solvent free neat conditions.

The CuO nanoparticles are recyclable upto 5th cycle without loss of significant reactivity (Table S9). After completion of the C–O cross-coupling of phenol with iodobenzene, the reaction mixture was treated with diethyl ether. Then, the overall mixture was centrifuged to isolate the catalyst. After isolation, it was washed with water and ether repeatedly and then dried for further use (Figure S13). The reusability tests indicate high yield. A comparative study with the bulk CuO synthesized by precipitation method was also studied – a lower amount of yield (~40%–55%) was obtained for CuO bulk.

The catalytic activity of our synthesized CuO-NPs was investigated for the cross-coupling of iodobenzene with phenol and compared with similar heterogeneous catalysts (Table S10). Unlike homogeneous catalyst, use of heterogeneous catalyst is much more advantageous in terms of their easy separation, recyclability, high thermal stability and longer lifetime. In this respect, based on literature and availability of the heterogeneous catalysts, the reactivity of ZnO, SnO, SnO₂, CuO, Cu₂O and CuO NPs/SiO₂ [37] has been judged and compared with respect to C–O coupling reaction of phenol and iodobenzene. Our synthesized CuO is found to be most effective with respect to yield of the desired coupling product. Heterogeneous catalysts other than CuO and Cu₂O found to be completely ineffective giving no yield of the desired C–O coupling product (entries 1–3).

A suitable mechanistic pathway for the above-mentioned catalysis reactions was proposed (Scheme S1). These results suggest that the reaction may occur by oxidative addition followed by reductive elimination. The oxidative addition of the aryl halide with catalyst can give intermediate **A**, which can undergo reaction with an alcohol or thiol to afford intermediate **B**. Intermediate **B** can provide the C–O or C–S cross coupling product by reductive elimination. According to Sambigioglio et al. the mechanism of such reactions is still unclear and it is considered that the mechanism actually varies depending on the substrate, ligand and reaction conditions [22b]. It is believed that the most active catalyst is Cu(I)-species which may form from the initial copper source.

Electrical Conductivity of MOF and MOF derived CuO-NPs: In complex **1**, the coordination between the metal centres and ndc²⁻ ligands forms 2D coordination layers and coordinated

1,10-phen moieties are hanging from the layers to connect next to neighbouring layers through $\pi \dots \pi$ interaction to form 3D supramolecular structure. Due to the presence of extended $\pi \dots \pi$ conjugation within the structure of **1**, we hope that the framework may show electrical conductivity. Bulk electrical conductivity of complex **1** has been measured by four probe contact using Ag wire on the pressed pellets. The conductivity of complex **1** is 3×10^{-3} S/cm at 312 K with Ohmic behaviour within the range of ± 40 V, Fig. 7(a and b). Variable temperature conductivity measurement within the temperature range of 312 K to 423 K indicates that with increasing temperature, conductivity of the framework increases – the framework is semiconducting in nature. The conductivity value is 4.2×10^{-3} S/cm at 423 K. With increasing temperature, delocalization of π -electrons increases and this may be a reason behind the linear rise in conductivity value electrical conductivity. The calculated activation energy of the framework is 0.077 eV.

Koo et al. have reported a semiconductive metal–organic framework having 2,5,8-tri(4-pyridyl)1,3-diazaphenylene as the π -conjugated ligand. Single crystal electrical conductivity measurement gives a value of $\sim 1 \times 10^{-6}$ S/cm [12a]. Kuang et al. have reported single crystal conductivity value of $\sim 1.2 \times 10^{-5}$ S/cm of a framework having naphthalenediimide [12b]. Haider et al. have measured conductivity on the single crystal of a framework containing 1,4,5,8-naphthalenetetracarboxylate and the framework shows conductivity of $\sim 10^{-4}$ S/cm [12c]. Chen et al. have reported the semiconducting behaviour of mixed metal MOF in which 4,4'-(anthracene-9,10-diylbis(ethyne-2,1-diyl))dibenzoate is used to induce $\pi \dots \pi$ interaction within the framework at separation distance of 3.4 Å [12d]. Electrical conductivity measurement on single crystals gives a conductivity value of 1.3×10^{-3} S/cm. Qu et al. have measured electrical conductivity of a metal–organic framework containing N,N'-di(4-pyridyl)-1,4,5,8-naphthalenetetracarbox-diimide on both single crystal and pressed pellets [12e]. Single crystal conductivity measurement showed 10^3 times higher conductivity (3.3×10^{-3} S/cm) than measured on the pressed pellets (7.6×10^{-6} S/cm). In our case, four probe electrical conductivity measurement on the pressed pellet of complex **1** gives a value of 3×10^{-3} S/cm at 312 K.

We have also studied the electrical conductivity of the MOF derived CuO-NPs in a similar manner. CuO is a p-type semiconductor but the bandgap and electrical conductivity vary with

the size and morphology of the nano-particles [38]. In most cases, the bandgap of CuO-NPs varies in the range of 1.2 to 2.0 eV and, based on its narrow bandgap, CuO-NPs have significant applications in electronic and opto-electronics. The conductivity of the MOF derived CuO-NPs is 4.85×10^{-2} S/cm with similar Ohmic behaviour at 312 K and this conductivity value is 16 times higher than the parent MOF, Fig. 7a and b. Combustion of the organic moieties within the MOF leads to the occurrence of charge transfer interaction between the copper and oxygen atoms within the framework and this may be the reason behind this enhanced conductivity. The variable temperature conductivity of the NPs is measured within the range of 312 to 588 K and the CuO-NPs also show semiconducting behaviour. The conductivity value rises smoothly up to 430 K (11×10^{-2} S/cm) and afterwards increases very rapidly to 1.11 S/cm at 588 K. A plot of $\ln(\sigma)$ vs. $1000/T$ for CuO-NPs shows two linear portions intersecting each other (Figure S14). This indicates the presence of two activation energy of CuO and values are 73 and 370 meV respectively, with a crossover at 430 K. The comparatively small activation energy indicates that Cu(I) and Cu(0) in association with oxygen vacancies may be present in CuO-NPs [16a]. Change of activation energy with temperature may be due to the presence of any metastable state in the sample.

4. Conclusions

Single crystal X-ray analysis of complex 1 revealed two types of binding modes (μ_2 - and μ_4 -) of ndc^{2-} ligands to the central Cu(II) ions, which, in turn, resulted in the formation of 2D coordination sheet. While the hanging 1,10-phenanthroline ligands in the interlamellar space assembled together by π - π interactions, which led to the formation of spongy 3D supramolecular metal-organic framework (MOF). Careful analysis of the MOF, which was stable up to 260 °C, depicted the presence of interpenetrated network topology. Reversible structural transformation of the framework by gliding motion of π - π stacked 1,10-phenanthroline ligands along the crystallographic a -axis and hence reversible expansion and contraction among the layer gap of 2D coordination sheets was confirmed by variable temperature PXRD measurements. Adsorption studies of the MOF with water, methanol and ethanol depicted a hysteresis loop in adsorption/desorption cycle. After thorough characterization of the MOF, it was calcinated at 650 °C for 4 h to fabricate CuO-NPs. The PXRD patterns confirmed the formation of CuO-NPs. While microscopic images showed formation of nearly uniform CuO-NPs with an average size of ~ 25 nm. Electrical conductivity measurements of the MOF and MOF derived CuO-NPs suggested both of them are semiconducting nature. However, CuO-NPs were found to be far more conducting compared to the parent MOF. Further, selective and efficient CuO-NPs catalyzed C-O and C-S bond-forming reaction of aryl iodides and various thiophenols is developed. This catalytic procedure offers general applicability and simplicity, avoiding the expensive and time-consuming preparation of suitable ligands and activated substrates. Based on controlled experiments and green chemistry rules, we proposed a solvent free, neat reaction conditions. Because of these advantages, we strongly believe that the protocol demonstrated in this work could find large application. And, we hope that such MOF derived nano-particle synthesis technique may be used for the synthesis of different types of metal-oxide nano-materials like ZnO, Cr_2O_3 , VO_2 , rare earth oxides.

CRediT authorship contribution statement

Maxcilian Patra: Synthesized the materials and carried out most of the experiments, Writing manuscript. **Soumen Kumar Dubey:** Synthesized the materials and carried out most of the experiments, Writing manuscript. **Bibhas Mondal:** Carried out all the catalysis experiments, Written the manuscript. **Kajal Gupta:** Carried out all the electrical conductivity measurements, Written the manuscript. **Angshuman Ghosh:** Carried out several characterizations like NMR, IR, Manuscript preparation. **Subhankar Mandal:** Carried out the XPS measurement, Manuscript preparation. **Satyajit Hazra:** Carried out the XPS measurement, Manuscript preparation. **Ajit Kumar Meikap:** Carried out all the electrical conductivity measurements, Written the manuscript. **Ujjal Kanti Roy:** Carried out all the catalysis experiments, Written the manuscript. **Subham Bhattacharjee:** Idea of this research project was drawn, Manuscript preparation. **Rajat Saha:** Idea of this research project was drawn, Manuscript preparation.

Declaration of competing interest

The authors declare that they have no known competing financial interests or personal relationships that could have appeared to influence the work reported in this paper.

Acknowledgements

This work was supported by funding from TARE, SERB to R. S. (TAR/2018/000744) and DST Inspire Faculty Research Grant to S.B. (Faculty Registration No.: IFA18-CH304, DST/INSPIRE/04/2018/000329). U.K.R. acknowledges financial support of this work by SERB New Delhi, SR/FT/CS-137/2011 dated 12.07.2012, and Science and Technology and Biotechnology-WB, 50 (Sanc.)/ST/P/S&T/15G-10/2018 dated 30.01.2019 to UKR is gratefully acknowledged. M. P. and S. K. D. thank DST Inspire Faculty Research Grant for financial assistance. The authors thank Goutam Sarkar for his technical support in XPS measurements. S. M. acknowledges the Council of Scientific & Industrial Research (CSIR), India for providing a research fellowship.

Appendix A. Supplementary data

Supplementary material related to this article can be found online at <https://doi.org/10.1016/j.nanoso.2021.100756>. The CCDC number is 2013885 for complex 1. Figure S1–S9, Table S1–S8, NMR spectra and catalytic mechanism scheme are given in Supporting information file.

References

- [1] (a) H. Furukawa, K.E. Cordova, M. O'Keeffe, O.M. Yaghi, The chemistry and applications of metal-organic frameworks, *Science* 341 (2013) 1230444.
- (b) R. Chakraborty, P.S. Mukherjee, P.J. Stang, Supramolecular coordination: self-assembly of finite two- and three-dimensional ensembles, *Chem. Rev.* 111 (2011) 6810.
- (c) T.K. Maji, R. Matsuda, S. Kitagawa, A flexible interpenetrating coordination framework with a bimodal porous functionality, *Nat. Mater.* 6 (2007) 142.
- (d) J.A. Mason, M. Veenstra, J.R. Long, Evaluating metal-organic frameworks for natural gas storage, *Chem. Sci.* 5 (2014) 32.
- (e) J.-R. Li, R.J. Kuppler, H.-C. Zhou, Selective gas adsorption and separation in metal-organic frameworks, *Chem. Soc. Rev.* 38 (2009) 1477.
- (f) A. Corma, H. García, F.X.L. Xamena, Engineering metal organic frameworks for heterogeneous catalysis, *Chem. Rev.* 110 (2010) 4606.
- (g) J.L.C. Rowsell, O.M. Yaghi, Metal-organic frameworks: a new class of porous materials, *Microporous Mesoporous Mater.* 73 (2004) 3.
- (h) S. Kitagawa, R. Kitaura, S. Noro, Functional porous coordination polymers, *Angew. Chem. Int. Ed.* 43 (2004) 2334.

- (i) W.P. Lustig, S. Mukherjee, N.D. Rudd, A.V. Desai, J. Li, S.K. Ghosh, Metal-organic frameworks: functional luminescent and photonic materials for sensing applications, *Chem. Soc. Rev.* 46 (2017) 3242.
- (j) A.M. Al-Enizi, J. Ahmed, M. Ubaidullah, S.F. Shaikh, T. Ahamad, M. Naushad, G. Zheng, Utilization of waste polyethylene terephthalate bottles to develop metal-organic frameworks for energy applications: A clean and feasible approach, *J. Clean. Prod.* 248 (2020) 119251.
- (k) A.M. Al-Enizi, M. Ubaidullah, J. Ahmed, T. Ahamad, T. Ahmad, S.F. Shaikh, M. Naushad, Synthesis of niox@ npc composite for high-performance supercapacitor via waste pet plastic-derived ni-mof, *Compos. B. Eng.* 183 (2020) 107655.
- (l) M. Ubaidullah, J. Ahmed, T. Ahamad, S.F. Shaikh, S.M. Alshehri, A.M. Al-Enizi, Hydrothermal synthesis of novel nickel oxide@ nitrogenous mesoporous carbon nanocomposite using costless smoked cigarette filter for high performance supercapacitor, *Mater. Lett.* 266 (2020) 127492.
- (m) N. Bakhtiari, S. Azizian, S.M. Alshehri, N.L. Torad, V. Malgras, Y. Yamauchi, Study on adsorption of copper ion from aqueous solution by mof-derived nanoporous carbon, *Microporous Mesoporous Mater.* 217 (2015) 173–177.
- (n) H. Zhang, M. Zhang, M.V. Lin Ping, J. Tang, S.M. Alshehri, Y. Yusuke, D. Shaowu, J. Zhang, A highly energetic n-rich metal-organic framework as a new high-energy-density, *Material. Chem. Eur. J.* 22 (2015) 1141–1145.
- [2] (a) N. Nidamanuri, K. Maity, S. Saha, Electrically conductive metal-organic frameworks, in: *Book Chapter, World Scientific Publishing*, 2017.
- (b) V. Stavila, A.A. Talin, M.D. Allendorf, Mof based electronic and opto-electronic devices, *Chem. Soc. Rev.* 43 (2014) 5994.
- [3] (a) E.M. Miner, T. Fukushima, D. Sheberla, L. Sun, Y. Surendranath, M. Dincă, Electrochemical oxygen reduction catalysed by Ni₃(Hexaiminotriphenylene)₂, *Nature Commun.* 7 (2016) 10942.
- (b) M.G. Campbell, D. Sheberla, S.F. Liu, T.M. Swager, M. Dincă, Cu₃(Hexaiminotriphenylene)₂: An electrically conductive 2D metal-organic framework for chemiresistive sensing, *Angew. Chem. Int. Ed.* 54 (2015) 4349.
- (c) J. Park, M. Lee, D. Feng, Z. Huang, A.C. Hinckley, A. Yakovenko, X. Zou, Y. Cui, Z. Bao, Stabilization of hexaaminobenzene in a 2D conductive metal-organic framework for high power sodium storage, *J. Am. Chem. Soc.* 140 (2018) 10315.
- (d) S. Roy, M. Das, A. Bandyopadhyay, S.K. Pati, P.P. Ray, T.K. Maji, Colossal increase in electric current and high rectification ratio in a photoconducting, self-cleaning, and luminescent schottky barrier nmof diode, *J. Phys. Chem. C* 121 (2017) 23803.
- (e) S.S. Shinde, C.H. Lee, J.-Y. Jung, N.K. Wagh, S.-H. Kim, D.-H. Kim, C. Lin, S.U. Lee, J.-H. Lee, Unveiling Dual-Linkage 3D Hexaiminobenzene Metal-Organic Frameworks towards Long-Lasting Advanced Reversible Zn-Air Batteries, *Energy Environ. Sci.* 12 (2019) 727.
- (f) D. Feng, T. Lei, M.R. Lukatskaya, J. Park, Z. Huang, M. Lee, L. Shaw, S. Chen, A.A. Yakovenko, A. Kulkarni, J. Xiao, K. Fredrickson, J.B. Tok, X. Zou, Y. Cui, Z. Bao, Robust and conductive two-dimensional metal-organic frameworks with exceptionally high volumetric and areal capacitance, *Nat. Energy* 3 (2018) 30.
- (g) D. Sheberla, J.C. Bachman, J.S. Elias, C.-J. Sun, Y. Shao-Horn, M. Dinca, Conductive MOF electrodes for stable supercapacitors with high areal capacitance, *Nat. Mater.* 16 (2017) 220.
- (h) X. Huang, S. Zhang, L. Liu, L. Yu, G. Chen, W. Xu, D. Zhu, Superconductivity in a copper(ii) based coordination polymer with perfect kagome structure, *Angew. Chem. Int. Ed.* 57 (2018) 146.
- [4] (a) S. Takaishi, M. Hosoda, T. Kajiwara, H. Miyasaka, M. Yamashita, Y. Nakanishi, Y. Kitagawa, K. Yamaguchi, A. Kobayashi, H. Kitagawa, Electroconductive porous coordination polymer Cu[Cu(Pdt)₂] composed of donor and acceptor building units, *Inorg. Chem.* 48 (2009) 9048.
- (b) Y. Kobayashi, B. Jacobs, M.D. Allendorf, J.R. Long, Conductivity, doping, and redox chemistry of a microporous dithiolene-based metal-organic framework, *Chem. Mater.* 22 (2010) 4120.
- [5] (a) M.E. Ziebel, L.E. Darago, J.R. Long, Control of electronic structure and conductivity in two-dimensional metal-semiquinoid frameworks of titanium, vanadium, and chromium, *J. Am. Chem. Soc.* 140 (2018) 3040.
- (b) S. Benmansour, A. Abherve, P. Gómez-Claramunt, C. Vallés- García, C.J. Gómez-García, Nanosheets of two-dimensional magnetic and conducting Fe(II)/Fe(III) mixed-valence metal-organic frameworks, *ACS Appl. Mater. Interfaces* 9 (2017) 26210.
- (c) J.A. DeGayner, I.-R. Jeon, L. Sun, M. Dincă, T.D. Harris, 2D conductive iron-quinoid magnets ordering up to T_c = 105 K via heterogenous redox chemistry, *J. Am. Chem. Soc.* 139 (2017) 4175.
- [6] (a) M.-H. Zeng, Q.-X. Wang, Y.-X. Tan, S. Hu, H.-X. Zhao, L.-S. Long, M. Kurmoo, Rigid pillars and double walls in a porous metal-organic framework: Single-crystal to single-crystal, controlled uptake and release of iodine and electrical conductivity, *J. Am. Chem. Soc.* 132 (2010) 2561.
- (b) X. Zhang, I. da Silva, R. Fazzi, A.M. Sheveleva, X. Han, B.F. Spencer, S.A. Sapchenko, F. Tuna, E.J.L. McInnes, M. Li, S. Yang, M. Schröder, Iodine adsorption in a redox-active metal-organic framework: electrical conductivity induced by host-guest charge-transfer, *Inorg. Chem.* 58 (2019) 14145.
- [7] (a) A.A. Talin, A. Centrone, A.C. Ford, M.E. Foster, V. Stavila, P. Haney, R.A. Kinney, V. Szalai, F.E. Gabaly, H.P. Yoon, F. Léonard, M.D. Allendorf, Tunable electrical conductivity in metal-organic framework thin-film devices, *Science* 343 (2014) 66.
- (b) C. Schneider, D. Ukaj, R. Koerver, A.A. Talin, G. Kieslich, S.P. Pujari, H. Zuilhof, J. Janek, M.D. Allendorf, R.A. Fischer, High electrical conductivity and high porosity in a Guest@MOF Material: Evidence of TCNQ Ordering within Cu₃BTc₂, *Micropores. Chem. Sci.* 9 (2018) 7405.
- [8] J.G. Park, M.L. Aubrey, J. Oktawiec, K. Chakarawet, L.E. Darago, F. Grandjean, G.J. Long, J.R. Long, Charge delocalization and bulk electronic conductivity in the mixed-valence metal-organic framework Fe(1, 2, 3-Triazolate)₂(BF₄)_x, *J. Am. Chem. Soc.* 140 (2018) 8526.
- [9] (a) L.S. Xie, G. Skorupskii, M. Dinca, Electrically conductive metal-organic frameworks, *Chem. Rev.* 120 (2020) 8536–8580.
- (b) X. Kuang, S. Chen, L. Meng, J. Chen, X. Wu, G. Zhang, G. Zhong, T. Hu, Y. Li, C.-Z. Lu, *Chem. Commun.* 55 (2019) 1643–1646.
- [10] (a) L. Sun, T. Miyakai, S. Seki, M. Dincă, Mn₂(2, 5-disulphydrylbenzene-1, 4-dicarboxylate): A microporous metal-organic framework with infinite (-Mn-S)-∞ chains and high intrinsic charge mobility, *J. Am. Chem. Soc.* 135 (2013) 8185.
- (b) F. Gándara, F.J. Uribe-Romo, D.K. Britt, H. Furukawa, L. Lei, R. Cheng, X. Duan, M. O'Keeffe, O.M. Yaghi, Porous, conductive metal-triazolates and their structural elucidation by the charge-flipping method, *Chem. Eur. J.* 18 (2012) 10595.
- [11] L. Liu, J.A. DeGayner, L. Sun, D.Z. Zee, T.D. Harris, Reversible redox switching of magnetic order and electrical conductivity in a 2D manganese benzoquinoid framework, *Chem. Sci.* 10 (2019) 4652.
- [12] (a) J.Y. Koo, Y. Yakiyama, G.R. Lee, J. Lee, H.C. Choi, Y. Morita, M. Kawano, Selective formation of conductive network by radical-induced oxidation, *J. Am. Chem. Soc.* 138 (2016) 1776.
- (b) X. Kuang, S. Chen, L. Meng, J. Chen, X. Wu, G. Zhang, G. Zhong, T. Hu, Y. Li, C.-Z. Lu, Supramolecular aggregation of a redox-active copper-naphthalenediimide network with intrinsic electron conduction, *Chem. Commun.* 55 (2019) 1643.
- (c) G. Haider, M. Usman, T.-P. Chen, P. Perumal, K.-L. Lu, Y.-F. Chen, Electrically driven white light emission from intrinsic metal-organic framework, *ACS Nano* 10 (2016) 8366.
- (d) D. Chen, H. Xing, Z. Su, C. Wang, Electrical conductivity and electroluminescence of a new anthracene-based metal-organic framework with π-conjugated zigzag chains, *Chem. Commun.* 52 (2016) 2019.
- (e) L. Qu, H. Iguchi, S. Takaishi, F. Habib, C.F. Leong, D.M. D'Alessandro, T. Yoshida, H. Abe, E. Nishibori, M. Yamashita, Porous molecular conductor: electrochemical fabrication of through-space conduction pathways among linear coordination polymers, *J. Am. Chem. Soc.* 141 (2019) 6802.
- [13] S.S. Park, E.R. Hontz, L. Sun, C.H. Hendon, A. Walsh, T. Van Voorhis, M. Dincă, Cation-dependent intrinsic electrical conductivity in isostructural tetrathiafulvalene-based microporous metal-organic frameworks, *J. Am. Chem. Soc.* 137 (2015) 1774.
- [14] P.I. Scheurle, A. Mähringer, A.C. Jakowetz, P. Hosseini, A.F. Richter, G. Wittstock, D.D. Medina, T. Bein, A highly crystalline anthracene-based MOF-74 series featuring electrical conductivity and luminescence, *Nanoscale* 11 (2019) 20949.
- [15] J.K. Sun, Q. Xu, Functional materials derived from open framework templates/precursors: Synthesis and applications, *Energy Environ. Sci.* 7 (2014) 2071.
- [16] (a) R. Das, P. Pachfule, R. Banerjee, P. Poddar, Metal and metal oxide nanoparticles synthesis from metal organic frameworks (MOFs): finding the border of metal and metal oxides, *Nanoscale* 4 (2012) 591.
- (b) S. Singha, A. Saha, S. Goswami, S.K. Dey, S. Payra, S. Banerjee, S. Kumar, R. Saha, A metal organic framework to CuO nanospheres of uniform morphology for synthesis of α-aminonitriles under solvent-free conditions along with crystal structure of the MOF, *Cry. Growth Des.* 18 (2018) 189.
- (c) S. Ekambaram, K.C. Patil, M. Maaza, Synthesis of lamp phosphors: facile combustion approach, *J. Alloys Compd.* 393 (2005) 81–92.
- (d) B.T. Sone, E. Manikandan, A. Gurib-Fakim, M. Maaza, Sm₂O₃ nanoparticles green synthesis via callistemon viminalis' extract, *J. Alloys Compd.* 650 (2015) 357–362.
- (e) S. Khamlich, E. Manikandan, B.D. Ngom, J. Sithole, O. Nemraoui, I. Zorkani, Synthesis, characterization, and growth mechanism of α-cr₂O₃ monodispersed particles, *J. Phys. Chem. Solids.* 72 (2011) 714–718.
- (f) S. Karthik, P. Siva, K.S. Balu, R. Suriyaprabha, V. Rajendran, M. Maaza, Acalypha indica-mediated green synthesis of ZnO nanostructures under differential thermal treatment: effect on textile coating, hydrophobicity, uv resistance, and antibacterial, *Adv. Powder Technol.* 28 (2017) 3184–3194.

- (g) N. Mayedwa, N. Mongwaketsi, S. Khamlich, K. Kaviyarasu, N. Matinise, Green synthesis of nickel oxide, palladium and palladium oxide synthesized via *Aspalathus linearis* natural extracts: physical properties & mechanism of formation, *Appl Surf Sci.* 446 (2018) 266–272.
- (h) H. Guo, T.T. Li, W.W. Chen, L.X. Liu, J.L. Qiao, J. Zhang, Self-assembly formation of hollow Ni-Fe-O nanocage architectures by metal-organic frameworks with high-performance lithium storage, *Sci. Rep.* 5 (2015) 13310, 5.
- (i) H.B. Wu, B.Y. Xia, L. Yu, X.-Y. Yu, X.W. Lou, Porous molybdenum carbide nano-octahedrons synthesized via confined carburization in metal-organic frameworks for efficient hydrogen production, *Nature Comm.* 6 (2015) 6512, 1.
- (j) P. Panchfule, X. Yang, Q. Zhu, N. Tsumori, T. Uchida, Q. Xu, From Ru nanoparticle-encapsulated metal-organic frameworks to highly catalytically active Cu/Ru nanoparticles-embedded porous carbon, *J. Mater. Chem. A* 5 (2017) 4835.
- (k) Z. Liang, C. Qu, D. Xia, R. Zou, Q. Xu, Atomically dispersed metal sites in MOF-based materials for electrocatalytic and photocatalytic energy conversion, *Angew. Chem. Int. Ed.* 57 (2018) 9604.
- [17] (a) R. Dai, W. Sun, Y. Wang, Ultrasmall tin nanodots embedded in nitrogen-doped mesoporous carbon: Metal-organic-framework derivation and electrochemical application as highly stable anode for lithium ion batteries, *Electrochim. Acta* 217 (2016) 123.
- (b) A.C. Nwanya, D. Obi, K.I. Ozoemena, R.U. Osuji, C. Awada, A. Ruediger, M. Maaza, F. Rosei, F.I. Ezema, Facile synthesis of nanosheet-like CuO film and its potential application as a high-performance pseudocapacitor electrode, *Electrochimica Acta* 198 (2016) 220–230.
- (c) B.T. Sone, A. Diallo, X.G. Fuku, A. Gurib-Fakim, M. Maaza, Biosynthesized CuO nano-platelets: physical properties & enhanced thermal conductivity nanofluidics, *Arab. J. Chem.* 13 (2020) 160–170.
- (d) A.C. Nwanya, M.M. Ndipingwi, N. Mayedwa, L.C. Razanamahandry, C.O. Ikpo, Maize (*zea mays* L.) fresh husk mediated biosynthesis of copper oxides: potentials for pseudo capacitive energy storage, *Electrochimica Acta* 301 (2019) 436–448.
- [18] H. Pang, B. Guan, W. Sun, Y. Wang, Metal-organic-frameworks derivation of mesoporous nio nanorod for high-performance lithium ion batteries, *Electrochim. Acta* 213 (2016) 351.
- [19] (a) J. Wu, Y. Song, R. Zhou, S. Chen, L. Zuo, H. Hou, L. Wang, Zn-Fe-ZIF-derived porous ZnFe₂O₄/C@NCNT nanocomposites as anodes for lithium-ion batteries, *J. Mater. Chem. A* 3 (2015) 7793.
- (b) W.J. Meng, W. Chen, L. Zhao, Y. Huang, M.S. Zhu, Y. Huang, Y.Q. Fu, F.X. Geng, J. Yu, X.F. Chen, Porous Fe₃O₄/carbon composite electrode material prepared from metal-organic framework template and effect of temperature on its capacitance, *Nano Energy* 8 (2014) 133.
- [20] C.F. Lee, Y.C. Liu, S.S. Badsara, Transition-metal-catalyzed C-S bond coupling reaction, *Chem. Asian J.* 9 (2014) 706.
- [21] (a) S.F. Nielsen, E.O. Nielsen, G.M. Olsen, T. Liljefors, D. Peters, Novel potent ligands for the central nicotinic acetylcholine receptor: Synthesis, receptor binding, and 3D-QSAR analysis, *J. Med. Chem.* 43 (2000) 2217.
- (b) G. De Martino, M.C. Edler, G. La Regina, A. Cosuccia, M.C. Barbera, D. Barrow, R.I. Nicholson, G. Chiosis, A. Brancale, E. Hamel, M. Artico, R. Silvestri, New arylthioindoles: potent inhibitors of tubulin polymerization. 2. structure-activity relationships and molecular modeling studies, *J. Med. Chem.* 49 (2006) 947.
- [22] (a) S.V. Ley, A.W. Thomas, Modern synthetic methods for copper-mediated C(aryl)-O, C(aryl)-N, and C(aryl)-S Bond Formation, *Angew. Chem. Int. Ed.* 43 (2003) 5400.
- (b) C. Sambiagio, S.P. Marsden, A.J. Blacker, P.C. McGowan, *Chem. Soc. Rev.* 43 (2014) 3525–3550.
- [23] T. Punniyamurthy, L. Rout, Recent advances in copper-catalyzed oxidation of organic compounds, *Coord. Chem. Rev.* 252 (2008) 134.
- [24] (a) K.E. Torraca, X. Huang, C.A. Parrish, S.L. Buchwald, An efficient intermolecular palladium-catalyzed synthesis of aryl ethers, *J. Am. Chem. Soc.* 123 (2001) 10770.
- (b) J. Mondal, A. Modak, A. Dutta, A. Bhaumik, Facile C-S coupling reaction of aryl iodide and thiophenol catalyzed by Cu-grafted furfural functionalized mesoporous organosilica, *Dalton Trans.* 40 (2011) 5228.
- (c) G.B.B. Varadwaj, S. Rana, K.M. Parida, Stable amine functionalized montmorillonite supported Cu, Ni catalyst showing synergistic and cooperative effectiveness towards C-S coupling reactions, *RSC Adv.* 3 (2013) 7570.
- (d) E. Sperotto, G.P.M. van Klink, J.G. de Vries, G. van Koten, Ligand-free copper-catalyzed C-S coupling of aryl iodides and thiols, *J. Org. Chem.* 73 (2008) 5625.
- [25] (a) G.T. Venkanna, H.D. Arman, Z.J. Tonzetich, Catalytic C-S cross-coupling reactions employing Ni complexes of pyrrole-based pincer ligands, *ACS Catal.* 4 (2014) 2941.
- (b) X. Xu, J. Liu, J.J. Zhang, Y.W. Wang, Y. Peng, Nickel-mediated inter- and intramolecular C-S coupling of thiols and thioacetates with aryl iodides at room temperature, *Org. Lett.* 15 (2013) 3, 550.
- (c) O. Bistri, A. Correa, C. Bolm, Iron-catalyzed C-O cross-couplings of phenols with aryl iodides, *Angew. Chem. Int. Ed.* 47 (2008) 586.
- [26] S. Mandal, M. Mukherjee, S. Hazra, Evolution of electronic structures of polar phthalocyanine substrate interfaces, *ACS Appl. Mater. Interfaces* 12 (2020) 45564–45573.
- [27] Bruker, APEX2, SAINT and SADABS, BRUKER AXS, Inc., Madison, Wisconsin, USA, 2008.
- [28] G.M. Sheldrick, Crystal structure refinement with SHELX, *Acta Cryst.* C71 (2015) 3–8.
- [29] L.J. Farrugia, Wingx and ORTEP for windows, an update, *J. Appl. Crystallogr.* 45 (2012) 849–854.
- [30] A.L. Spek, Structure validation in chemical crystallography, *Acta Cryst.* D65 (2009) 148–155.
- [31] L.J. Farrugia, ORTEP-3 for windows - a version of ORTEP-III with a graphical user interface (GUI), *J. Appl. Crystallogr.* 30 (1997) 565.
- [32] X. He, C. Lu, D. Yuan, L. Chen, Q. Zhang, C. Wu, Hydrothermal synthesis, crystal structures, and properties of a class of 2D coordination polymers, *Eur. J. Inorg. Chem.* (2005) 4598.
- [33] (a) R. Kitaura, K. Seki, G. Akiyama, S. Kitagawa, Porous coordination-polymer crystals with gated channels specific for supercritical gases, *Angew. Chem. Int. Ed.* 42 (2003) 428.
- (b) J. Zhang, S. Kitagawa, Supramolecular isomerism, framework flexibility, unsaturated metal center, and porous property of Ag(I)/Cu(I) 3, 3', 5, 5'-tetramethyl-4, 4'-bipyrazolate, *J. Am. Chem. Soc.* 130 (2008) 907.
- [34] T.K. Maji, M. Ohba, S. Kitagawa, Transformation from a 2D stacked layer to 3D interpenetrated framework by changing the spacer functionality: Synthesis, structure, adsorption, and magnetic properties, *Inorg. Chem.* 44 (2005) 9225.
- [35] M.C. Biesinger, Advanced analysis of copper X-ray photoelectron spectra, *Surf. Interface Anal.* 49 (2017) 1325–1334.
- [36] (a) X. Lv, W. Bao, *J. Org. Chem.* 72 (2007) 3863.
- (b) D. Ma, Q. Cai, N, N-dimethyl glycine-promoted ullmann coupling reaction of phenols and aryl halides, *Org. Lett.* 5 (2003) 3799.
- (c) H.-J. Cristau, P.P. Cellier, S. Hamada, J.-F. Spindler, M. Taillefer, A general and mild ullmann-type synthesis of diaryl ethers, *Org. Lett.* 6 (2004) 913.
- (d) S. Jammi, S. Sakthivel, L. Rout, T. Mukherjee, S. Mandal, R. Mitra, P. Saha, T. Punniyamurthy, Cu nanoparticles catalyzed c-n, c-o and c-s cross coupling reaction: scope and mechanism, *J. Org. Chem.* 74 (2009) 1971–1976.
- [37] A.R. Hajipour, F. Dordahan, F. Rafiee, M. Mahdavi, C-n cross-coupling reaction catalysed by efficient and reusable CuO/SiO₂ nanoparticles under ligand-free conditions, *Appl. Organ. Chem.* 28 (2014) 809–813.
- [38] S. Sagadevan, P. Murugasen, Electrical properties of copper oxide nanoparticles, *J. Nano Res.* 30 (2015) 1.



Cite this: *CrystEngComm*, 2021, 23, 3510

Photo-responsive Schottky diode behavior of a donor–acceptor co-crystal with violet blue light emission†

Soumen Singha,^a Rajkumar Jana,^{ab} Rituparna Mondal,^{ac} Partha Pratim Ray,^a Partha Pratim Bag,^{id} Kajal Gupta,^e Nandan Pakhira,^e Corrado Rizzoli,^f Arabinda Mallick,^{id} Sanjay Kumar^{id}*^a and Rajat Saha^{id}*^{ae}

Herein, we report the crystal structure, supramolecular structure, electronic transport properties and optoelectronic behaviour of a co-crystal made of tetrabromoterephthalic acid (TBTA) and quinoxaline (QUIN) (1 : 1). The sample has been characterized using thermogravimetric analysis and spectral techniques. Moreover, theoretical analyses of noncovalent interactions, optical properties and the band structure of the co-crystal have been performed. The co-crystal has been crystallized in an orthorhombic system with the *Pnma* space group and the constituent molecules assemble in the solid state by using O–H···N hydrogen bonding, $\pi\cdots\pi$, Br··· π and Br···O interactions. The ground state geometry optimization over the hydrogen bonded dimer by DFT method indicates that TBTA acts as the donor and QUIN as the acceptor within the self-assembled co-crystal. According to UV-vis spectroscopic study the bandgap of the co-crystal is ~ 3.18 eV. In the solid state it exhibits a broad emission band with a maximum at 405 nm while in aqueous medium its photoluminescence emission peaks are obtained at 350 and 403 nm. The values of the average fluorescence lifetime of the sample in aqueous medium are 3.38 ns at 352 nm and 4.94 ns at 403 nm. Under UV-irradiation, the co-crystal emits violet-blue light. The emission spectrum in solution phase shows a relative quantum yield of 0.018. Band structure calculation indicates that the co-crystal is a p-type semiconductor with a bandgap of 2.835 eV. Due to its semiconducting character, the ITO/co-crystal/Al sandwiched structured device acts as a Schottky barrier diode with rectification ratio, ideality factor, barrier height and series resistance of 41, 1.36, 0.70 eV, and 26.97 k Ω , respectively. The current through the device increases substantially under visible light exposure. Upon visible light illumination the values of electrical conductivity, mobility and carrier concentration increase by 35 (± 0.5), 54 (± 0.5) and 6 (± 0.5)%, respectively, with respect to dark conditions. It has been shown that $\pi\cdots\pi$ and hydrogen bonding interactions can play a crucial role in producing the donor–acceptor (D–A) type co-crystal, semiconducting behaviour can be incorporated in the organic co-crystal utilizing $\pi\cdots\pi$ and hydrogen bonding interactions and weak intermolecular $\pi\cdots\pi$, Br··· π and Br···O interactions can act as the pathway for electrical conduction.

Received 5th January 2021,
Accepted 2nd March 2021

DOI: 10.1039/d1ce00020a

rsc.li/crystengcomm

Introduction

In recent times, photo-responsive organic semiconductors¹ have attracted enormous attention because of their significant application potential in photodetectors,² optical switches,³ LED⁴ and photovoltaic cells.⁵ In this context, donor–acceptor molecular co-crystals connected by charge transfer and weak intermolecular interactions like hydrogen bonding⁶ and π -interactions⁷ which also have success in crystal engineering have emerged as the most promising material of this category.^{8–11} The physicochemical properties of co-crystals are poles apart from the sum of their components. These properties can be tuned rationally by altering intermolecular interactions through judicious selection of the constituents. Recently, study of the semiconducting and optoelectronic

^a Department of Physics, Jadavpur University, Jadavpur, Kolkata-700032, WB, India. E-mail: kumars@phys.jdvu.ac.in, rajatinorg1@gmail.com

^b Department of Physics, Techno India University, EM-4, Sector-V, Salt lake, Kolkata-700091, India

^c Department of Electronics, Barrackpore Rastraguru Surendranath College, Barrackpore, West Bengal 700120, India

^d Dumka Engineering College, Dumka, Jharkhand-814101, India

^e Department of Chemistry, Kazi Nazrul University, Asansol-713340, WB, India

^f Dipartimento SCVSA, Università di Parma, Parco Area delle Scienze 17/A, Parma, Italy

† Electronic supplementary information (ESI) available: Experimental procedures, tables, relevant figures and other related documents. CCDC 1841621. For ESI and crystallographic data in CIF or other electronic format see DOI: 10.1039/d1ce00020a

behaviour of organic co-crystals/salts has attracted paramount attention due to their enormous application possibilities in next generation environment friendly electronic and optoelectronic devices in place of the Si-based devices used nowadays.^{12–36} However, very few co-crystals exhibit photo-responsive properties.^{15–36} Thorough investigation of the electronic and optoelectronic properties of a number of organic co-crystal based devices fabricated in laboratory conditions yielded very promising results in respect to their application possibilities in the area of light emitting diodes,¹⁷ light emitting transistors,^{18,19} lasers,²⁰ photoconductors,^{21,22} and photovoltaic cells.²³

Tsutsumi *et al.*, have reported the photovoltaic behaviour of a device fabricated by using DBTTF–TCNQ (dibenzotetrathiofulvalene–tetracyanoquinodimethane) co-crystal with narrow bandgap (0.7 eV).²⁴ The thin film solar cell made of tetracene-doped anthracene co-crystal exhibits an optical efficiency of 23.72%.²⁵ The highest power conversion efficiency achieved in fullerene and squaraine co-crystal based heterojunction solar cells is 10%.²⁶ The organic p–n junction photovoltaic cell made from contorted hexabenzocoronene (donor) and spherical fullerene (acceptor) exhibits a good response but large scale production of the device has not yet been taken up due to lack of proper structural characterization of the co-crystal used.²⁷ W. Hu and co-workers have assessed the optoelectronic performance of several D–A type charge transfer co-crystals.^{28–32} They have examined morphology dependant photo-responsive behaviour of two different co-crystals of perylene (P) and TCNQ (T) and shown that the on–off photocurrent ratios of the devices made of 1:1 and 3:1 P–T co-crystals under visible light illumination are 5.4 and 4.4, respectively.³⁰ In another article, they have shown that the bipyridylethylene (BPE)–1,2,4,5-tetracyanobenzene (TCNB) co-crystal can be used as an optical waveguide.³¹ They have also designed photonic logic gate properties of an organic co-crystal composed of 4-(1-naphthylvinyl)pyridine and 1,2,4,5-tetracyanobenzene.³² The field effect transistor (FET) fabricated by using the co-crystal of C₆₀ and 5,10,15,20-tetrakis(3,5-dimethoxyphenyl)porphyrin (3,5-TPP) responds to NIR radiation.³³ The heterojunction device made from the acridine–trimesic acid co-crystal exhibits an ultrahigh on–off photocurrent ratio of the order of 10⁴.³⁴ The electrical conductivity of co-crystal of 1,3,6,8-pyrenetetrasulfonic acid tetrasodium salt as donor and 1,1'-bibutyl-4,4'-bipyridinium dibromide as acceptor increases upon illumination with laser beam of wavelength 405 nm.³⁵ However, this co-crystal has low conductivity.³⁵

Earlier we have reported the role of weak intermolecular interactions (like hydrogen bonding, π – π , Br \cdots π and Br \cdots O interactions) in the electrical response of tetrabromoterephthalic acid (TBTA) based multi-component semiconducting co-crystals through formation of Schottky barriers.³⁶ Recently, we have reported the photo-responsive behaviour of some organic co-crystal/salts based Schottky barrier diodes.¹⁵ It is noteworthy that the weak intermolecular

interactions between the donor and acceptor molecules of co-crystals can be utilized for generation of photocarriers.^{1,5,15–23} Thus, from a fundamental view point of crystal engineering it appears that the possibility of forming a co-crystal utilizing charge transfer/ π – π stacking between TBTA and quinoxaline (QUIN) molecules and having the supramolecular network formed by weak hydrogen bonding, π – π , Br \cdots π and Br \cdots O interactions can be explored in order to examine the role of such weak noncovalent interactions in the electronic transport properties and optoelectronic behaviour through a comprehensive study of the photo-responsive properties of a TBTA–QUIN based Schottky barrier diode.

Herein, we have designed a semiconducting-luminescent co-crystal of the poly-bromo organic molecule TBTA as donor and QUIN as acceptor (Fig. S1†) using the solvent evaporation method, characterized it using single crystal X-ray diffraction (SCXRD), UV-vis, luminescence lifetime measurements and fluorescence microscopic imaging techniques. Its photo-responsive properties have also been examined. Structural study reveals that this TBTA–QUIN co-crystal has been formed by the self-assembly of its constituents TBTA and QUIN through hydrogen bonding and π – π interactions and it has assembled in the solid state through supramolecular O–H \cdots N hydrogen bonding, Br \cdots O, Br \cdots π and π – π interactions. Theoretical inspection of the energy levels of frontier molecular orbitals of the hydrogen bonded dimer shows that TBTA acts as donor while QUIN acts as acceptor. Band structure calculations show that the bandgap of the co-crystal is 2.835 eV and this value agrees well with the optical bandgap (3.18 eV) obtained from solid state UV-vis spectra. Under UV-irradiation the co-crystal emits violet-blue light. To examine the electrical response, thin film of the co-crystal is fabricated on an ITO surface and the ITO/co-crystal/Al sandwich structure exhibits “Schottky diode” behaviour with a rectification ratio of 45 in dark conditions. The conductivity of the co-crystal made device increases by 35 (± 0.5)% upon visible light exposure and it exhibits “Schottky diode” behaviour with a rectification ratio of ~ 56 .

Experimental section

This study includes the solvent evaporation synthesis of TBTA–QUIN co-crystal, X-ray single crystal structural characterization, density functional theory (DFT) based calculation of the binding energy and non-covalent interactions within the components, Hirshfeld surface analysis, spectroscopic study and its theoretical verification by DFT and periodic DFT calculations (details are provided in the ESI†). The *I*–*V* measurements in dark and under visible light illumination have been performed on an Al/co-crystal/ITO sandwich structure fabricated by using an SCU 2700 spin coating system. Aluminium (Al) electrode is deposited on the active thin film by a vacuum coating unit (12A4D of HINDHIVAC) using a shadow mask. The *I*–*V* characteristics, in dark and under visible light irradiation, of the co-crystal have been recorded using the two probe method using a

Keithley 2400 sourcemeter interfaced with a PC at applied bias voltage in the range of -2 to $+2$ V. The I - V measurements have been carried out in a dark box. The photo-responsive behaviour of the device has been investigated under AM 1.5 G photo-irradiation. Details of the I - V measurements are provided in the ESI†

Results and discussion

Molecular and supramolecular structure of the co-crystal

Upon mixing equimolar ethanolic solutions of TBTA and QUIN (Fig. 1) the co-crystal was grown *via* the solvent evaporation method. Rhombohedral shaped (Fig. S1†) colourless single crystals were collected and characterized using the single crystal X-ray crystallographic technique (ESI†). Structural analysis reveals that the co-crystal crystallizes in the orthorhombic system with *Pnma* space group (Tables 1 and S1†). The asymmetric unit of the co-crystal contains half of each of the TBTA and QUIN molecules (Fig. S2†). In the molecule of TBTA, the carboxylic groups are almost perpendicular (angle between the plane of the phenyl ring and the plane of carboxylic acid group is 87.23° , Fig. S3†) to the plane of the phenyl ring. The C–O bond lengths (O1–C5 = $1.302(3)$ Å, O2–C5 = $1.192(3)$ Å) confirm the presence of the carboxylic acid group. The QUIN moiety is completely planar and is co-planar to the phenyl ring of the TBTA moiety.

Interestingly, the TBTA and QUIN molecules are connected by O–H \cdots N hydrogen bonds to form the 1D supramolecular chains along the *b*-axis (Fig. 2, S4 and Table S2†). Two parallel 1D chains are connected by $\pi\cdots\pi$ interactions (Fig. S5 and Table S3†) between the TBTA and QUIN molecules to form a double layer which is further connected by Br \cdots O interactions (Fig. S6 and Table S4†) to form a 2D supramolecular structure within the *ab*-plane (Fig. 2). These 2D sheets are further bridged by Br $\cdots\pi$ interactions (Table S5†) to form a 3D supramolecular network (Fig. S7†).

PXRD, thermal and IR analyses

The phase purity of the bulk material was characterized by PXRD analysis (Fig. S8†). Thermal analysis reveals two-step degradation of the co-crystal. The sample is stable up to 140 °C, and then for the 1st step of decomposition within the temperature range 140 – 220 °C the weight loss of the sample is nearly 24.5% indicating the removal of the QUIN moiety from the structure. In the next step the remaining part of the sample gets completely degraded in the temperature interval

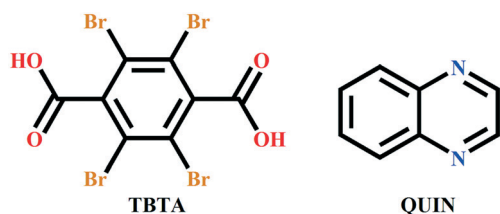


Fig. 1 Molecular structures of co-crystallizing components.

Table 1 Crystallographic data of the TBTA–QUIN co-crystal

Structure	Crystal form
System	Orthorhombic
Space group	<i>Pnma</i>
<i>a</i> (Å)	9.4972(18)
<i>b</i> (Å)	14.745(3)
<i>c</i> (Å)	13.181(2)
α (°)	90
<i>V</i> (Å ³)	1845.8(6)
Z, density	4, 2.202
CCDC no.	1841621

of 270 – 360 °C (Fig. S9†). The vibrational spectra recorded in ATR mode (Fig. S10†) show shifts in the frequency band positions corresponding to C=O and O–H vibrations in the co-crystal with respect to TBTA towards lower frequencies. This may be attributed to the weakening of C=O and O–H vibrations due to intermolecular hydrogen bonding interactions between TBTA and QUIN in the co-crystal.

Inspection of noncovalent interactions within the co-crystal

Hirshfeld surface analysis

The Hirshfeld surface analysis provides more detailed information regarding the intermolecular interactions and the 2D fingerprint plot quantifies these interactions within the crystal structure (details are provided in the ESI†). The Hirshfeld surfaces were calculated over TBTA molecules (Fig. 3) and the 2D fingerprint plots (Fig. S11†) were analysed accordingly. The d_{norm} surface of TBTA was mapped over the fixed colour scale of -0.751 to 1.417 Å. It displays some bright circular red spots, which correspond to the short intermolecular O \cdots H and N \cdots H interactions. The light red spots correspond to the long intermolecular Br \cdots O, Br $\cdots\pi$, C \cdots H and H \cdots H interactions. The 2D fingerprint plots reveal that the O \cdots H interactions comprise 17.0% of the total Hirshfeld surface and appear as a blunt spike with the lowest contact distance $d_i \approx 1.5$ Å and $d_e \approx 1.3$ Å. The N \cdots H

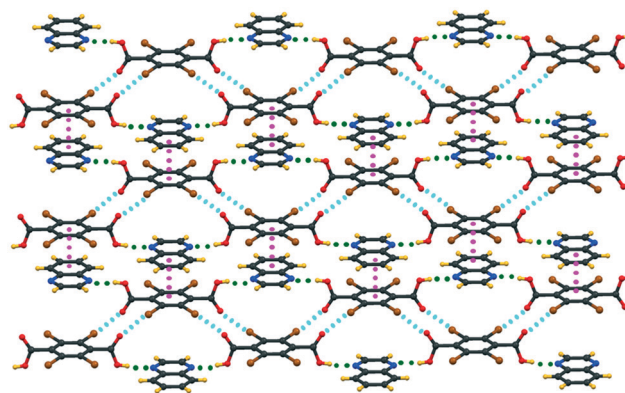


Fig. 2 2D supramolecular structure formed by hydrogen bonds (green), halogen bonds (cyan) and $\pi\cdots\pi$ interactions (magenta).

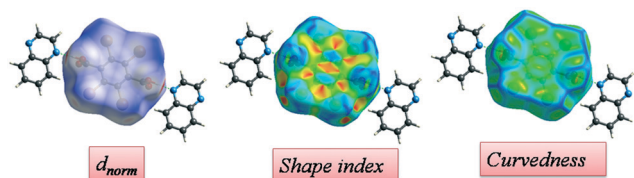


Fig. 3 Hirshfeld d_{norm} , shape index and curvedness surfaces of TBTA-QUIN around TBTA.

interactions cover 4.3% of the total surface and emerge as a sharp spike with contact distance $d_i \approx 0.6 \text{ \AA}$ and $d_e \approx 1.0 \text{ \AA}$. The $\text{Br}\cdots\text{C}$ interaction corresponding to $\text{Br}\cdots\pi$ comprises 13.5% of the surface and appears as two spikes with average contact distance $d_e + d_i \approx 3.4 \text{ \AA}$. The $\text{C}\cdots\text{H}$, $\text{Br}\cdots\text{O}$, $\text{H}\cdots\text{H}$ and $\text{Br}\cdots\text{H}$ interactions are found in the 2D fingerprint plot with relative surface areas 2.3%, 18.4%, 7.1% and 27.4%, respectively as shown in Fig. S10.†

Intermolecular interaction energies

The quantitative view of the topology of the distribution of overall interaction energies sustaining the molecular components within the crystal structure have been calculated by two ways. Firstly on the basis of pair-wise interaction energies by summing up four energy components *viz.*, electrostatic (E_{el}), polarization (E_{pol}), dispersion (E_{dis}) and exchange repulsion (E_{rep}) on a structure-cluster mapped within 6 \AA in the neighbourhood of each component (TBTA and QUIN) of the co-crystal to include long-range interactions. Secondly the binding energies of the four kinds of self-assembled dimeric model geometries focussing

different kinds of intermolecular interactions (Fig. 4) were calculated from the difference of the energy of the system and the sum of individual components in the framework of DFT with counterpoise correction.

For a cluster of molecules within the $2 \times 2 \times 2$ unit cell, graphical representation of the individual energy components has been simulated in the energy framework and is depicted in Fig. S12.† The interactions for different kinds of orientations of the component molecules within the crystals have been explored in the energy framework and are presented in Fig. S13–S15.† The electrostatic and dispersion energies coexisting together provide the total interaction energy for the self-assembly of the co-crystal. Signatures of electrostatic force due to the strong $\text{O}\cdots\text{H}\cdots\text{N}$ hydrogen bonded arrays and dispersion force due to π -stacking interactions, $\text{Br}\cdots\text{O}$ halogen bonding with $\text{Br}\cdots\pi$ and $\text{C}\cdots\text{H}\cdots\pi$ interactions within the constituents of the heterodimers have been detected in the interaction energy plots (Fig. S13 and S14.†). The $\text{Br}\cdots\text{O}$ halogen bonding interactions between the TBTA homodimer have been detected to form a 2D-planar geometry made of a $R_2^2(10)$ network between the TBTA molecules (Fig. S15.†).

On the other hand Fig. 4(a) describes the binding energy of the first model dimer considering only the $\text{O}\cdots\text{H}\cdots\text{N}$ hydrogen bonding interactions, the second model (Fig. 4(b)) gives the binding energy of the weakly interacting π stacked dimer, the third and fourth models diagnose the intermolecular interactions between the homo-dimers, $\text{Br}\cdots\text{O}$ and $\text{Br}\cdots\pi$ interactions between two TBTA moieties (Fig. 4(c)) and $\text{C}\cdots\text{H}\cdots\pi$ interactions between two QUIN moieties (Fig. 4(d)). The calculated values of these interactions as listed in Table 2 show comparable results.

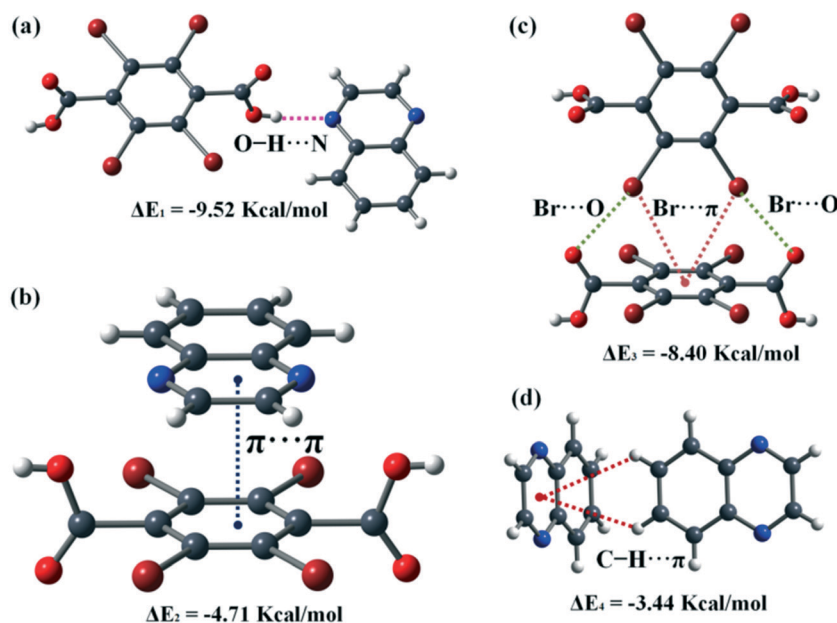


Fig. 4 Theoretical model geometries with the synthon energies describing (a) $\text{O}\cdots\text{H}\cdots\text{N}$ hydrogen bonding interaction, (b) $\pi\cdots\pi$ interaction for the TBTA-QUIN hetero-dimer model structures, (c) $\text{Br}\cdots\text{O}$ and $\text{Br}\cdots\pi$ interactions within the TBTA homo-dimer and (d) $\text{C}\cdots\text{H}\cdots\pi$ interactions between the QUIN homo-dimer model structure.

Table 2 Comparison between interaction energies calculated from the energy framework and binding energies from DFT computation

Pair	Interaction	Interaction energy	Binding energy
TBTA–QUIN heterodimer	O–H \cdots N hydrogen bonding interactions	–50.5 kJ mol $^{-1}$	–9.52 kcal mol $^{-1}$
	$\pi\cdots$ stacking interactions	–36.5 kJ mol $^{-1}$	–4.71 kcal mol $^{-1}$
TBTA homodimer	Br \cdots O halogen bonding with Br $\cdots\pi$	–31.4 kJ mol $^{-1}$	–8.40 kcal mol $^{-1}$
QUIN homodimer	C–H $\cdots\pi$ interactions	–11.6 kJ mol $^{-1}$	–3.44 kcal mol $^{-1}$
TBTA homodimers with R $_2^2(10)$ network forming a 2D-planar geometry	Br \cdots O halogen bonding interaction between the TBTA homodimers	–19.0 kJ mol $^{-1}$	

QTAIM and NCI plot analysis

A qualitative analysis of the topological properties of the noncovalent interactions prevailing within the dimer geometries based on the electron density has been performed using the quantum theory of atoms in molecules (QTAIM). In the QTAIM distribution of critical points (CPs) and bond paths each noncovalent interaction is characterized by a bond CP (yellow sphere) and bond path interconnecting the atoms of two different molecular units and to visualize the nature of the noncovalent interactions (NCI), the reduced density gradient (RDG) has been represented by iso-density surfaces over the interacting dimers (Fig. 5). The nature of the interaction between the molecules within the dimer can be traced through a red–blue–green colour scheme on the calculated iso-surface where blue colour usually highlights strong attractive interaction whereas red points towards strong repulsive interaction. Weak interactions (attractive) are indicated by green colour.

Fig. 5(a) shows the QTAIM representation of the heterodimer, where the O–H \cdots N hydrogen bond is portrayed by the bond critical point (BCP) represented by a yellow sphere and the bond path shown by a pink line interconnecting the H and N atoms. The small blue iso-surface located between the H and N atoms shows the NCI plot representation which confirms the presence of strong O–H \cdots N hydrogen bonding interactions. Fig. 5(b) displays several BCPs connecting the π -systems of both the QUIN

rings and the TBTA molecule, characterizing the π -stacking interaction. The extended green iso-surface between the π -stacked hetero-dimers indicates the weakly attractive nature of the interactions between the participating residues.

It can be observed that for the self-assembled homo-dimer (Fig. 5(c)) the distribution of bond critical points (CPs) and bond paths reveals two different types of interaction, one corresponds to the XB, where the Br and O atoms are interconnected by a bond CP and bond path and the other contact can be defined as a Br $\cdots\pi$ interaction that is characterized by a bond CP and bond path connecting the Br atom to one C-atom of the π -aromatic ring. The natures of weakly interacting Br \cdots O and Br $\cdots\pi$ interactions are characterized by three separate green iso-surfaces between them. On the other hand Fig. 5(d) presents the similar distribution of bond critical points (CPs) and bond paths, revealing the C–H $\cdots\pi$ short contacts by a bond CP and bond path interconnecting the H atom to one C-atom of the π ring of QUIN. The strength of the interaction can be observed by four discrete green iso-surfaces between the QUIN homodimer and was found to be weak in nature.

Optical, electronic and electrical transport properties

Spectroscopic and light emitting behaviour

The optical properties of the co-crystal have been examined in both solid state and aqueous medium (Fig. 6). The solid state absorption spectrum of the co-crystal shows a broad band in the UV region while in the aqueous medium multiple peaks appear (Fig. 6(a)). The peaks obtained at lower wavelength can be attributed to π – π^* transition while higher wavelength peaks are due to inter-ligand charge transfer (ILCT) between different moieties of the co-crystal. Usually, in the UV-vis reflectance spectra the band for the co-crystal formed by the charge transfer (CT) interaction appears at lower energy with respect to its individual components.¹² However, in the present case no such shifting of the band for the co-crystal has been observed, which discards the possibility of the presence of CT interaction between TBTA and QUIN moieties in the co-crystal (Fig. S16(a)†). The absorption spectra of the co-crystal in both solid state and solution phase show two major bands. The solution phase spectrum is blue shifted with respect to the solid state spectrum. The peaks in solution phase absorption spectrum are clearly resolved whereas for the solid state spectrum the

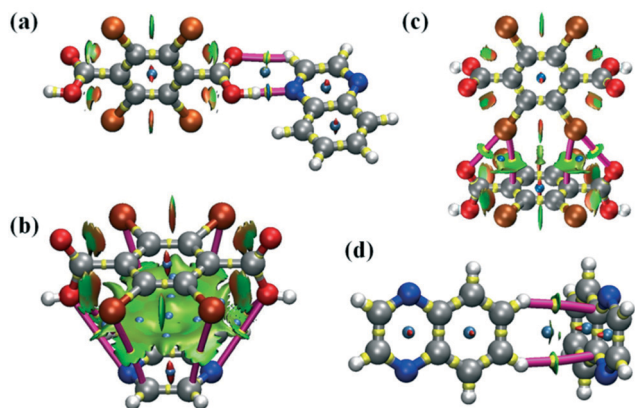


Fig. 5 AIM distribution of bond and ring critical points (yellow and tan spheres respectively), bond paths (magenta lines) and the nature of non-covalent interactions for the model dimeric geometries revealing (a) O–H \cdots N strong H-bonding interaction, (b) π -stacking interaction, (c) Br \cdots O and Br $\cdots\pi$ interactions and (d) C–H $\cdots\pi$ short contacts.

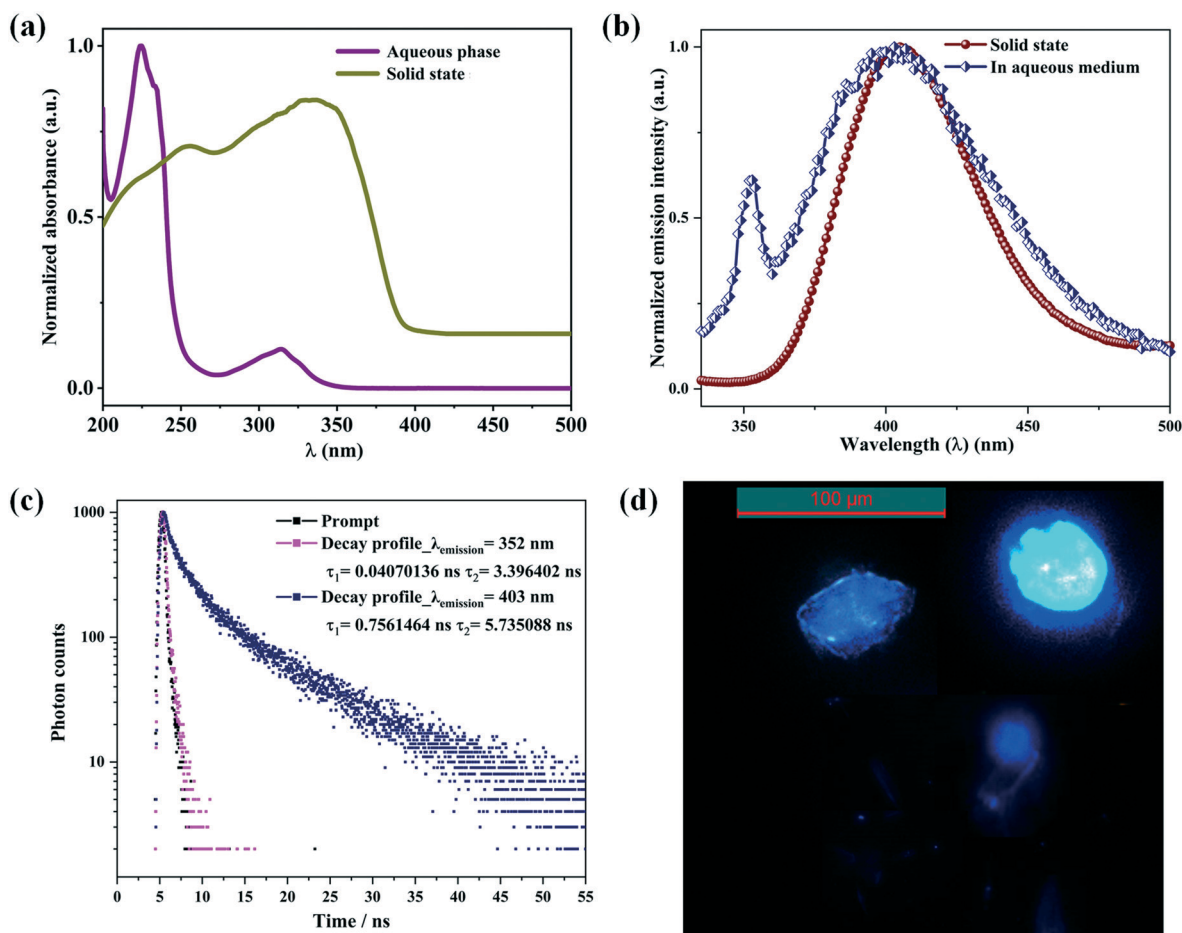


Fig. 6 (a) UV-vis absorption spectra of the sample in both solid state and aqueous medium, (b) steady state emission spectra of the sample in both solid state and aqueous medium ($\lambda_{\text{ex}} = 313 \text{ nm}$, conc. = $10^{-4} \text{ mol l}^{-1}$), (c) lifetime profile of the sample in solution phase and (d) fluorescence image of the co-crystal. The spectra of the sample in solid state and in solution phase as shown in Fig. 6(a) and (b) are normalized to illustrate their differences.

band nature can be observed, which mainly arises due to the aggregation effect. Fig. S16(b)† depicts the absorption behaviour of the sample and its components in solution phase. By correlating the experimental and simulated absorption spectra of the sample in solution phase it has been shown that the co-crystal retains its supramolecular assembly in the aqueous medium (see ESI†).

The solid state emission spectrum of the co-crystal shows a broad band with a maximum at 405 nm while in aqueous medium it has two peaks with maxima at 350 nm and 403 nm (Fig. 6(b)). Such behaviour is due to the solid state aggregation effect within the multi-component material. Concentration dependent absorption and emission spectra of the sample have also been studied in solution phase (Fig. S17(a) and (b)†). With increasing concentration, the intensity of the peaks in the absorption spectra increases continuously; while in the emission spectra, the intensity of the peak at 350 nm decreases and it increases for the peak at 403 nm. Most probably self-assembled aggregation is responsible for the decrement and the incessant increase in the propensity of the inter-ligand charge transfer interaction

with increasing concentration causes the significant enhancement in the intensity of the second peak.

Fluorescence lifetime is a very effective tool for probing the local environment around a fluorescent molecule and excited state interactions. The decay profiles of the sample recorded in aqueous environment have been fitted with a double-exponential (Fig. 6(c)) and the respective lifetime values τ_1 and τ_2 are provided in Table 3. The average lifetime values of the material in aqueous medium for those emission maxima were determined from the results of the time-resolved fluorescence spectroscopy using the equation: $\langle \tau_{\text{av}} \rangle = (a_1\tau_1^2 + a_2\tau_2^2)/(a_1\tau_1 + a_2\tau_2)$, where a_1 , a_2 are the percentage contributions for these two lifetime values and are presented in Table 3.

The relative quantum yield (Φ_{F}) calculation from the luminescence measurement carried out in solution phase (considering only the area under the emission spectrum with maximum at 403 nm) using quinine sulfate (QS) in 0.1 M H_2SO_4 as the standard reference shows that the sample is minimally radiative with $\Phi_{\text{F}} = 0.018$. The consequential radiative and non-radiative transition rate constants for this

Table 3 Lifetime values of the sample in aqueous environment

Monitoring wavelength (λ_{em})	a_1	τ_1 (ns)	a_2	τ_2 (ns)	$\langle\tau_{av}\rangle$ (ns)
352	0.17	0.04	0.83	3.39	3.38
403	0.59	0.75	0.41	5.73	4.94

a_1 , a_2 : percentage contributions for lifetime values; τ_1 , τ_2 : lifetime; and $\langle\tau_{av}\rangle$: average lifetime.

emission peak were extracted from the relations $k_r = \phi_F/\tau_{av}$ and $k_{ir} = (1 - \phi_F)/\tau_{av}$, respectively, and these values are found to be $k_r = 3.64 \times 10^6 \text{ s}^{-1}$ and $k_{ir} = 9.96 \times 10^8 \text{ s}^{-1}$. The fluorescence microscopic image of the co-crystal under UV irradiation has been recorded (Fig. 6(d)). The co-crystal shows violet-blue emission from its edges as expected from the coordinate (0.151, 0.056) of the CIE chromaticity diagram ((Fig. S18(c)†) drawn from the solid state PL spectra.

Ground state structural and electronic properties

The molecular structure of the co-crystal has been optimized in the electronic ground state (S_0) in both the gaseous phase and in water medium employing the DFT method with the 6-311++G(d,p) basis set. The gas phase and solution phase optimized geometries of the co-crystal are presented in Fig. S18† and the coordinates are reported in Tables S6 and S7.† As the present sample is not a CT type co-crystal and the hydrogen bonding interaction is the strongest interaction between the components of the co-crystal, the hydrogen bonded heterodimer was chosen as the molecular unit of the co-crystal for all molecular level calculations. In the starting solid state geometry derived from the crystal structure a molecular unit of the co-crystal contains a TBTA and a QUIN moiety where the carboxylic groups of TBTA are perpendicular to the aromatic ring of TBTA and the aromatic ring of TBTA is coplanar with the QUIN ring. The relative orientations of the different fragments of the optimized geometry in the aqueous phase is almost the same as the solid state molecular structure. The slight difference between these conformations is because of the presence of solvent interactions in the aqueous phase. On the other hand, for the optimized geometry in the gaseous phase the aromatic ring of the TBTA molecule becomes perpendicular with respect to the QUIN moiety and the carboxylic groups turn coplanar with the QUIN moiety. Due to the absence of crystalline packing force the optimized geometry of the molecule in the gaseous phase exhibits such a substantially different conformation from the solid state molecular geometry. Except for the bonds with H atoms all the optimized bond lengths are within the appreciable limit of $\sim 0.02 \text{ \AA}$. In the solution phase optimized geometry the increment of the O–H bond dimension is more than the gaseous phase optimized geometry. Some of the selected bond lengths of the co-crystal are listed in Table S8.†

The isodensity surface plots (isodensity = 0.02 e Bohr^{-3}) of some of the selected frontier molecular orbitals (FMO) of

both the optimized structures of the co-crystal along with their orbital energies are depicted in Fig. 7. For the FMOs the contributions coming from different parts of the co-crystal in terms of atomic contribution are obtained by the fragment analysis method, and energies of the FMOs along with the HOMO–LUMO energy differences are provided in Table S9.† It can be clearly seen that the FMOs for the geometries optimized in the gaseous phase and in water medium have different energies and the electron density distributions of the FMOs (Fig. 7) show different distribution of the isodensities over different parts of the molecules.

In the hydrogen bonded dimer the HOMO e-density is found over TBTA and the LUMO e-density is on QUIN for both the phases. Therefore for the ground state of the TBTA–QUIN self-assembly, TBTA will act as donor, whereas QUIN will act as acceptor. This observation is further supported by the calculation of the Mulliken charges over the atoms of the hydrogen bonded dimer geometry (Tables S10 and S11†). It may be noted that for both the phases all virtual orbitals subsequent to the LUMO are composed of contributions from a single entity. For both the phases, LUMO+1 to LUMO+3 are composed of the contribution from the TBTA moiety and LUMO+4 is composed of the sole contribution from the QUIN moiety. The HOMO–2 and HOMO–4 orbitals in the gaseous phase optimized structure and the HOMO–1 orbital in the aqueous medium optimized geometry are composed of sole contributions from the QUIN moiety. For all other occupied orbitals both the TBTA and QUIN moieties contribute in different ratios. All the % contributions are listed in Table S9.†

Singlet excited states and calculated absorption spectra

We have computed the theoretical UV-vis spectra of the co-crystal in both the gaseous state and aqueous medium using the ground state optimized geometries in the respective phases, with the help of the non-equilibrium approach of the time dependent density functional (TD-DFT) method. The energy of each excited state (S_n) represents the vertical excitation energy in electron volts (eV) from the ground state (S_0).

The theoretically (both in the gaseous and solution phases) and experimentally obtained UV-vis spectra of the co-crystal in aqueous medium are presented in Fig. 8. The absorption spectra of the co-crystal show multiple transitions and these excitations are primarily attributed to charge transfer transition between different moieties within the molecular unit of the co-crystals. The peaks in the experimental spectrum have been assigned by visual inspection. The values of theoretically calculated excitation wavelengths matching with experimental result, excitation energies, oscillator strengths and CI coefficients along with the corresponding most relevant transitions involved are presented in Tables S12 and S13.† Both the experimental and calculated spectral features of the co-crystal are more or less similar and lie in the UV region of the spectrum, except the fact that in the theoretical spectra there is a slight bathochromic shift relative to the experimental spectrum in the lower wavelength region.

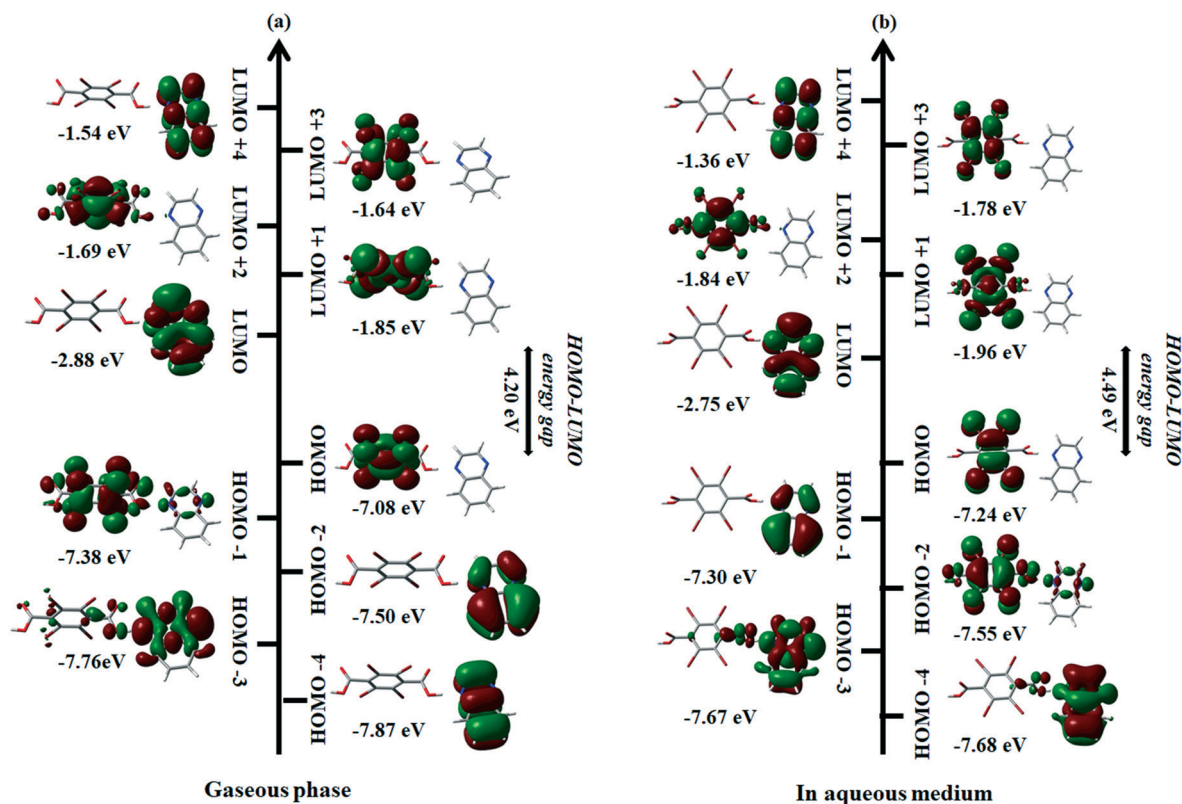


Fig. 7 Schematic representations of the selective FMOs of the co-crystal (a) in gaseous phase and (b) water medium.

The natural transition orbital (NTO) analysis based on the calculated transition density matrices allows us to identify and visualize the electronic transitions in terms of excitation from hole to electron of the singlet excitons. Further, the transition orbitals provide a graphical real-space representation of the transition densities associated with the molecular electronic excitations computed within the

framework of TD-DFT. The NTOs of the co-crystal for the gaseous phase and water medium excitations are depicted in Fig. S19 and S20.† The experimental transition wavelength, most appropriate theoretical transitions and corresponding hole and electron NTOs involved along with the weights of the respective configuration λ ($\lambda \leq 1$, where the parameter λ actually refers to the fraction of the NTO pair contribution to a given electronic excitation) have been pictorially provided in Fig. S19 and S20.† These calculated NTOs corresponding to the main absorption band clearly indicate the π - π^* character of these transitions. Both the hole and electron orbitals are spread over the different parts of the co-crystal, establishing a generalised characteristic π (for holes) and π^* (for electrons) nature of orbitals.

In Fig. S19† the lowest energy transition observed around 315 nm is found at *ca.* 308.49 nm (4.02 eV, $f = 0.0349$), which can be described by one set of NTOs (each with $\lambda = 0.98$) and is exclusively attributed to the π (QUIN) \rightarrow π^* (QUIN) ILCT transition. The next UV transition observed near 294 nm is computed at 282.18 nm (4.39 eV, $f = 0.0861$) and can be ascribed to π (QUIN) \rightarrow π^* (QUIN) ILCT transition. The most intense transition obtained \sim 237 nm is calculated at 232.75 nm (5.33 eV, $f = 0.2717$). This transition is due to n (N-QUIN) + π (TBTA) \rightarrow π^* (TBTA) ILCT transition in association with a slight LLCT nature. The most appropriate calculated transition near the experimentally observed transition at 225 nm is found at 218.82 nm (5.67 eV, $f = 0.2295$). This transition has both LLCT and ILCT characters and can be

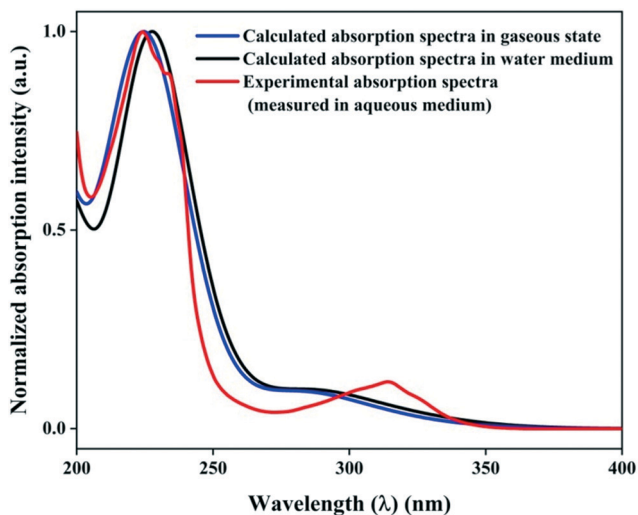


Fig. 8 Experimental absorption spectrum in aqueous medium along with the calculated absorption spectra in gaseous phase and water medium for the co-crystal at room temperature.

represented by π (TBTA + QUIN) \rightarrow π^* (TBTA) LLCT/ILCT transition. The experimentally observed UV-vis transitions of the co-crystal in water medium are theoretically interpreted in a similar manner and the results are summarized in Fig. S20.† So, the TD-DFT with NTO analysis establishes the excitations occurring due to inter/intra-molecular charge transfer interactions between TBTA and QUIN.

Electronic band structure and comparison with optical bandgap

The calculated band structure of the co-crystal along the high symmetry points of the 1st Brillouin zone is represented in Fig. 9(a) (and S21†). It shows that the bandgap of the co-crystal is 2.835 eV, which is close to the value of the optical bandgap (\sim 3.179 eV) calculated from the absorption band edge of the solid state UV-vis spectra (Fig. 9(b)). The dispersions in the valence and conduction bands are clearly described in Fig. 9(a). The parameters corresponding to the band structure are given in Table S14.† The lowest energy (2.835 eV) of the CBs is located at the *G* point (CBM), whereas, the highest energy (0.000 eV) of the VBs is localized at the *Z* point (VBM). This indicates that this co-crystal is an indirect bandgap semiconductor. The calculated band gap shows a slightly smaller value compared to the experimental optical bandgap which is again a general flaw of DFT calculations with the GGA functional. So it can be said without ambiguity that the co-crystal is an indirect band *p*-type semiconductor with a wide bandgap.

Now, the bands can be assigned according to total and partial densities of states (DOS) as depicted in Fig. S22.† The resonance of C-2s, O-2s, N-2s and Br-4s states in conjunction with a partial amount of H-1s, C-2p, N-2p and O-2p states construct the VB located in the range -24.2 eV to -10.5 eV. The bottom portion of the VB is mainly dominated by the

contribution from O-2p (21.4 electrons per eV) and N-2p (7.8 electrons per eV) orbitals. The next region above it is formed by C-2s (18.27 electrons per eV) and Br-4s (12.5 electrons per eV) orbitals. The top of the VB just below the Fermi level between the energy range -10.2 eV to the Fermi level (0.0 eV) are formed by the superposition of C-2p (35.8 electrons per eV) and Br-4p (30.70 electrons per eV) states in association with a considerable amount of contribution from N-2p (8.90 electrons per eV), O-2p (24.90 electrons per eV) and H-1s states. The topmost level of the VB (VBM ~ -1.02 eV \sim 0 eV) is formed due to the resonance of C-2p, N-2p and Br-4p orbitals. The conduction band (CB) just above the Fermi level ranging from 2.83 eV to 5.7 eV is formed due to the superposition of C-2p, N-2p and Br-4p orbitals mixing with a slight amount of O-2p orbitals where the states C-2p (8.35 electrons per eV) and N-2p (6.87 electrons per eV) dominate the bottom of the CB. The states C-2p and Br-4s mixing with a small amount of C-2s and H-1s have created the region ranging from 5.8 eV to 18.9 eV in the CB.

The partial density of state (PDOS) contribution of the two molecular units TBTA and QUIN in the total density of states for the co-crystal is depicted in Fig. S23.† In the PDOS, some peaks appearing at the same energy level (hybridization) for different atomic orbitals (Fig. S22†) and for different molecular fragments (Fig. S23†) clearly show the evidence of strong intermolecular interactions between the moieties of the co-crystal and intramolecular interactions within the moieties. The N-2p orbits hybridize with H-1s due to the resonance in peak positions from -13.5 eV to 0 eV implying partial charge transfer from H atoms to N atoms. So, the presence of strong H bonds between H atoms and N atoms is ensured. Again, a strong resonance is observed between the O-2p and Br-4p peaks within the range -7.9 eV to 0.0 eV. This can be argued to be the evidence of the presence of strong Br \cdots O halogen interaction between the non-bonded atoms.

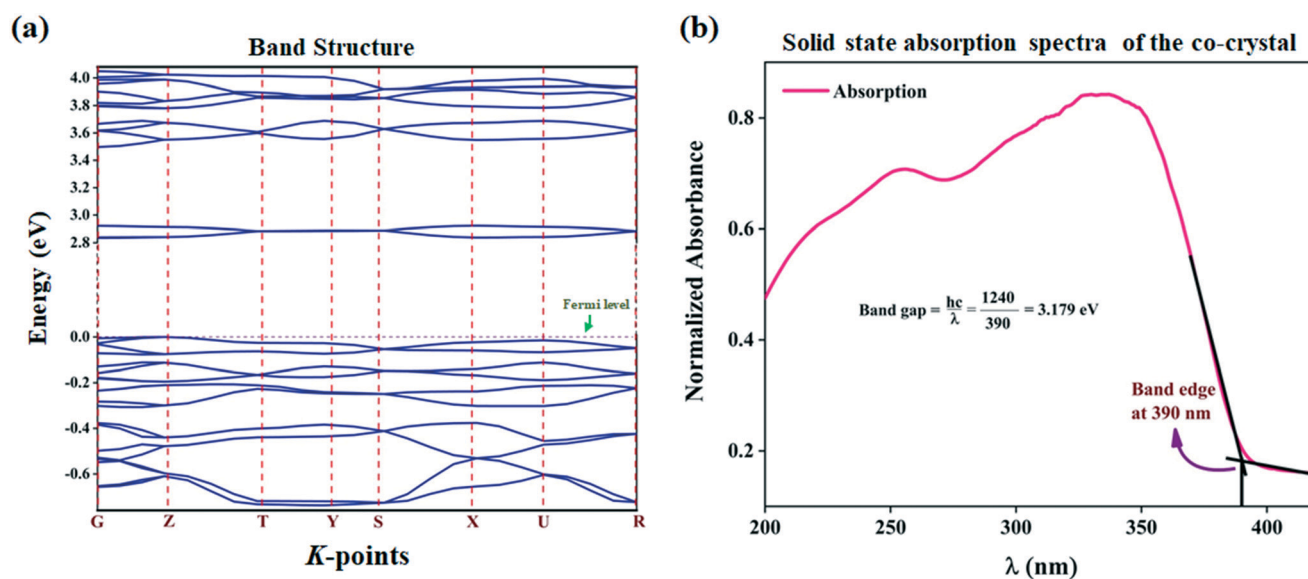


Fig. 9 (a) Calculated band structure zoomed in over the top of the VBs and bottom of CBs and (b) solid state UV-DRS spectrum of the co-crystal in the wavelength range 200 to 420 nm.

Optical properties from the electronic band structure

The electronic band structure calculation can provide insight regarding the optical response. The salient features of the parameters: real ($\varepsilon'(\omega)$) and imaginary ($\varepsilon''(\omega)$) parts of dielectric permittivity, reflectivity ($R(\omega)$), refractive index ($n(\omega)$), extinction coefficient ($k(\omega)$), optical conductivity ($\sigma(\omega)$), absorption coefficient ($\alpha(\omega)$) and energy-loss function ($L(\omega)$) as a function of frequency of the incident photon are displayed in Fig. 10 in the energy range 0–45 eV.

The plots of $\varepsilon''(\omega)$ and $\varepsilon'(\omega)$ against photon energy are shown in Fig. 10(a). The characteristic spectra for the $\varepsilon''(\omega)$ of the co-crystal comprise mainly four sharp peaks at 2.97, 7.12, 11.61 and 14.26 eV together with some shoulder peaks near 17.40 eV and beyond. At low frequency, the imaginary part $\varepsilon''(\omega)$ is zero and the threshold energy for the $\varepsilon''(\omega)$ is consistent with the bandgap of the material at equilibrium. At higher frequency (>35 eV), the $\varepsilon''(\omega)$ approaches to zero. The value of the static dielectric constant ($\varepsilon_s = \varepsilon'(0)$) is 2.98. The $\varepsilon'(\omega)$ fluctuates with increasing frequency and shows four peaks at 2.37, 6.11, 10.76 and 13.16 eV and afterward it starts decreasing, becoming negative in the energy range 19.20–24.32 eV which may be due to the metallic character of the sample in this energy range. At

higher energy, the value of $\varepsilon'(\omega)$ again turns positive and is almost independent of energy ($\varepsilon'(\infty) \sim 0.80$).

The reflectivity spectrum of the sample as displayed in Fig. 10(b) shows two distinct peaks: one sharp and strong peak at 6.92 eV and another weak peak at 2.46 eV. A broad band appears in the energy range 9 to 29 eV due to the superposition of several peaks located at 11.66, 14.78, 19.74 and 23.42 eV (accompanied by a shoulder). The reflectivity of the material approaches to zero when the frequency reaches near 45 eV. The zero energy value of reflectivity (*i.e.*, $R(0)$) is 7% and up to 4.83 eV the value of the reflectivity remains within 8.8%. Due to such a low value of reflectivity, the compound is nearly transparent in the infrared and visible energy range. Now, materials with a low refractive index are suitable for application in optoelectronic devices such as LEDs and solar cells. In the entire frequency range, the calculated value of the reflectivity of the co-crystal is lower than that in inorganic compounds like the metal oxides and thus it can be used for fabricating optoelectronic devices. The highest value of reflectivity (21.08%) is observed at 23.42 eV. It has been observed that the reflectivity value attains maximum when the value of $\varepsilon'(\omega)$ becomes negative (Fig. 10(a) and (b)).

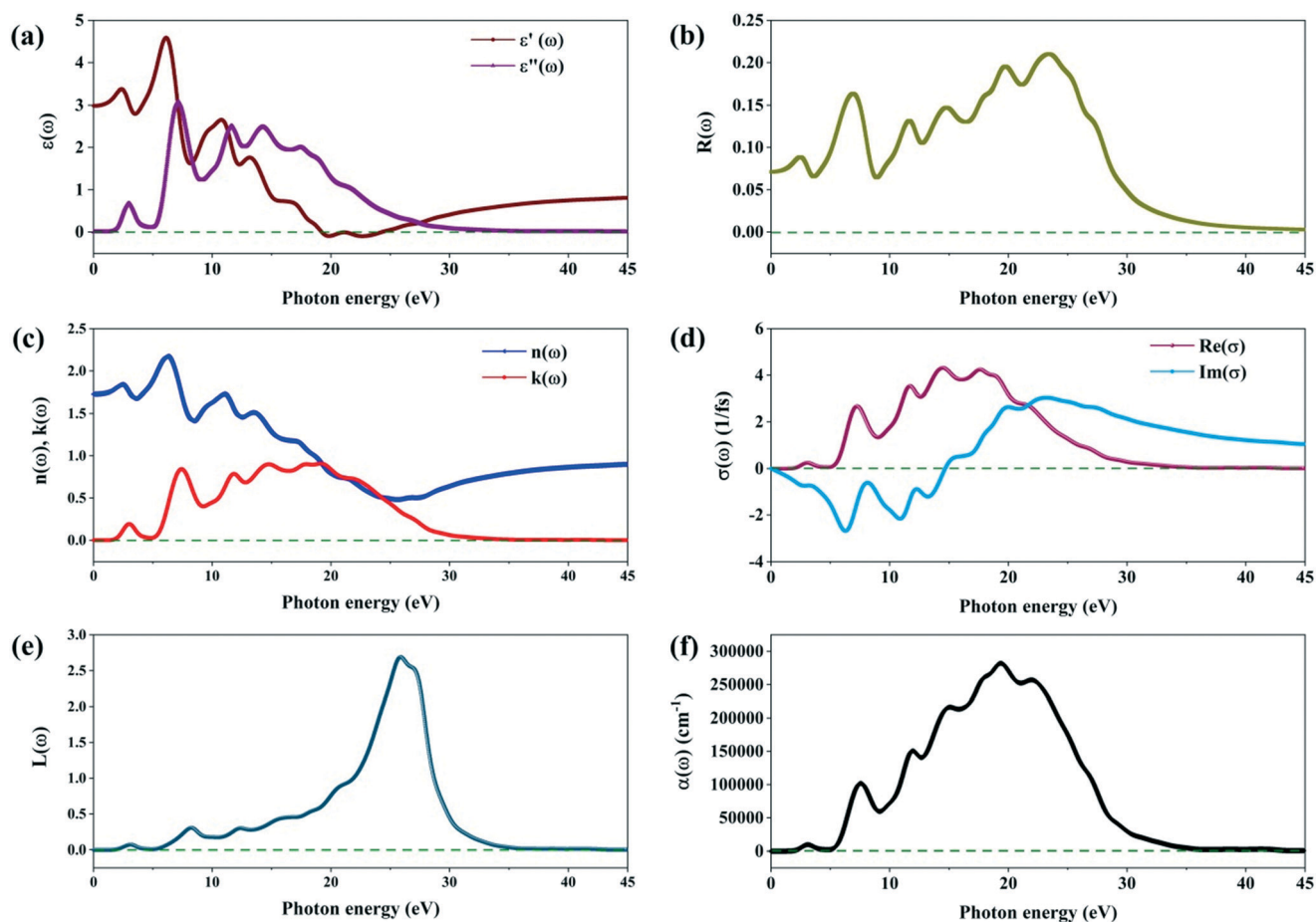


Fig. 10 The plot for (a) dielectric permittivity $\varepsilon(\omega)$; (b) reflectivity $R(\omega)$; (c) refractive index $n(\omega)$ and extinction coefficient $k(\omega)$; (d) optical conductivity $\sigma(\omega)$; (e) energy loss function $L(\omega)$ and (f) absorption coefficient $\alpha(\omega)$ of the co-crystal as a function of photon energy.

The co-crystal shows a non-zero value of refractive index $n(\omega)$ up to 45 eV (Fig. 10(c)). The value of $\varepsilon'(\omega)$ at zero energy ($\varepsilon'(0) = 2.98$) could be used to estimate the refractive index $n(\omega)$ at zero energy using the relationship $n(0) = [\varepsilon'(0)]^{1/2}$ and the estimated value of the static refractive index $n(0)$ for the co-crystal is found to be 1.73. From its zero energy value, the refractive index increases with frequency, reaching the maximum value of 2.17 at 6.23 eV. A value for the refractive index of more than one signifies that when the photons traverse through the material they get slowed down due to their interactions with the electrons. The extinction coefficient $k(\omega)$ (the imaginary part of the complex refractive index) shows two sharp peaks at 3.02 and 7.42 eV and satellite peaks at 11.84, 14.76, 17.94 and 19.13 eV to form a broad band. The $\varepsilon''(\omega)$ and $k(\omega)$ spectra display similar trends (Fig. 10(a) and (c)). The optical conductivity $\sigma(\omega)$ spectrum of the co-crystal is shown in Fig. 10(d). The real part of the complex conductivity exhibits peaks at 3.06, 7.24, 11.70 and 14.46 eV along with shallow shoulders located in the high energy region (~ 17.60 eV). The maximum value of the conductivity of the co-crystal was achieved at 14.46 eV with a magnitude of 4.32 1/fs.

The energy-loss function $L(\omega)$ (Fig. 10(e)) is an important optical parameter describing the energy loss of a fast moving photon traversing through a material. The peaks in the $L(\omega)$ spectrum represent the characteristics associated with the plasma resonance and the corresponding frequency is called the plasma frequency above which the material is a dielectric insulator [$\varepsilon'(\omega) > 0$] and below which the material behaves as a metal [$\varepsilon'(\omega) < 0$]. For this material the resonant energy loss is manifested by a strong band situated in the energy region 22 to 28 eV composed of peaks located at 20.84 (low intensity), 25.86 (intense peak) and 26.83 eV (shoulder). This region of plasma resonance corresponds to the region in which $\varepsilon'(\omega)$ is negative. Again, the peak for the plasma resonance associated with the $L(\omega)$ spectrum coincides with the trailing edges in the reflectivity spectra. The $\alpha(\omega)$ and $R(\omega)$ spectra are similar in the energy range 2.84 to 45 eV (Fig. 10(f)). In the low energy region distinct sharp peaks are observed at 3.10 and 7.55 eV followed by a strong broad band in the high energy region consisting of peaks located at 11.93 and 15.07 eV with the largest peak at 19.38 eV accompanied by two shoulder peaks at about 18.16 and 21.94 eV.

Electrical transport properties

According to UV-vis spectroscopic study and band structure calculation the co-crystal is a p-type semiconductor. So, to assess the electrical transport properties of the sample we have measured the current–voltage (I – V) characteristics of a device made of an ITO/co-crystal/Al sandwich structure (Fig. 11(a)) at room temperature. The I – V measurements have been performed in the applied bias voltage range from -2 to $+2$ V using the two-probe technique with the help of a Keithley 2400 source meter. The SEM micrograph of the active thin film of the co-crystal cast on the ITO surface is shown in Fig. 11(b).

The I – V characteristic curves of the device in the dark and under visible light illumination are presented in Fig. 11(c). The forward current of the device rises rapidly in a nonlinear fashion while it is very low and remains almost constant in the reversed bias region. The device is displaying rectifying behaviour with on/off ratios of 41 and 56 at ± 2 V in the dark and under visible light exposure, respectively. Thus, it is acting like a Schottky barrier diode due to the presence of the semiconducting co-crystal between the electrodes. Further, in the voltage range 0 to 0.8 V (region I) the I – V curves of the device under dark conditions and visible light illumination obey the equation $I = C_1 \exp(-C_2[\exp(C_3V) - 1])$, where C_1 , C_2 and C_3 are constants that depend on different parameters of the device, portraying the thermionic emission behaviour of a Schottky barrier diode whereas in the voltage range 0.8 to 2 V (region II) they follow the power law behaviour ($I \propto V^n$, with $n = 2$), manifesting that the space charge limited current (SCLC) controls the electrical transport mechanism of the device in this region (Fig. S25†). This clearly indicates that the device is a Schottky barrier diode.³⁶ Accordingly, we have analyzed region I using thermionic emission theory to determine the different parameters of the device while in region II, SCLC theory has been employed to estimate the electrical transport parameters of the device.

The values of the ideality factor (η), series resistance (R_s) and barrier height (ϕ_b) of the device have been calculated by analyzing the I – V curve of the device in region I in the framework of the model proposed by S. K. Cheung and N. W. Cheung³⁷ following the methodology reported earlier (details are provided in the ESI†). The effective charge carrier mobility (μ_{eff}), transit time (τ) and carrier concentration (n) of the device have been estimated using the Mott–Gurney law in the SCLC region (region II) following the standard approach described in the literature (details are provided in the ESI†) and utilizing the capacitance *versus* frequency plot of the device (Fig. S26†).^{38–40} The values of all the parameters of the device are listed in Table 4. The value of η deviates from its ideal value of unity due to the presence of the series resistance, existence of the interface states and the barrier inhomogeneities.^{41,42} Under light exposure, the values of μ_{eff} and n are increased by 54 (± 0.5)% and 6 (± 0.5)%, respectively, compared to those under dark conditions.

In dark conditions the value of electrical conductivity of the device is found to be $0.56 \times 10^{-5} \text{ S m}^{-1}$ and it increases to $0.76 \times 10^{-5} \text{ S m}^{-1}$ under light illumination (Table 4). The photo-responsive behaviour of the device has been verified by measuring the transient photocurrent of the device at 2 V under an illumination of 100 mW cm^{-2} . Fig. 11(d) represents the photocurrent (dark currents subtracted) *versus* time graph of the device. The device shows fast and reproducible photo-switching behaviour with light on and off (Fig. 11(d)). Photosensitivity (S) is an important parameter of photosensitive electronic devices and it is calculated with the help of the relationship, $S = (I_L - I_D)/I_D$ (ref. 43) where I_D and I_L are the dark current and photocurrent at $+2$ V, respectively. The value of S is calculated as 0.45.

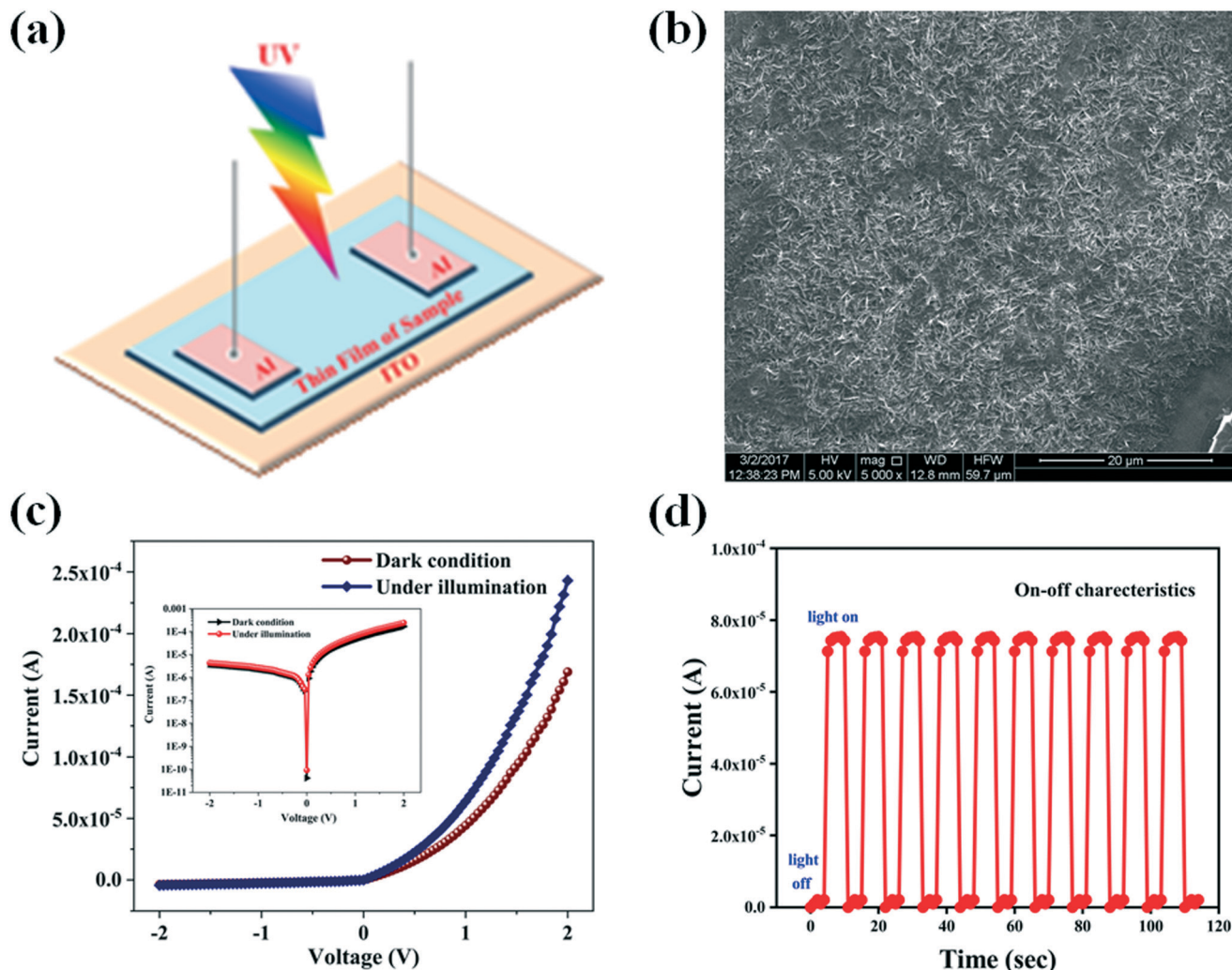


Fig. 11 (a) Schematic representation of the device, (b) SEM micrograph of the semiconducting layer, (c) photoconductive behaviour of the co-crystal, (d) on-off characteristics of the device.

Table 4 Important electrical and charge transport parameters of the Al/co-crystal/ITO device

Condition	On/off	S	η	R_s (k Ω)		Φ_b (eV)	$\sigma \times 10^{-5}$ (s m ⁻¹)	$\mu_{\text{eff}} \times 10^{-7}$ (m ² V ⁻¹ S ⁻¹)	$\tau \times 10^{-7}$ (S)	$n \times 10^{20}$ (eV m ⁻³)
				dV/dln I vs. I	$H(I)$ vs. I					
Dark	41	0.45	1.36	26.97	26.50	0.70	0.56	4.44	3.9	3.57
Light	56		1.19	19.72	18.77	0.65	0.76	6.86	2.7	3.79

S : photosensitivity, η : ideality factor, R_s : series resistance, Φ_b : barrier height, σ : conductivity, μ_{eff} : mobility, τ : transit time, n : carrier concentration.

To the best of our knowledge, this is a unique report of a donor-acceptor co-crystal based photo-responsive Schottky barrier diode. The co-crystal acts as a semiconductor because of the presence of weak intermolecular interactions, more specifically π - π interactions, between the donor and acceptor molecules of the co-crystal, which helps in generation of carriers. It may be noted that the conductivity, mobility and carrier concentration of the device increase substantially under visible light illumination compared to the dark condition. This indicates that the co-crystal responds toward the visible light by generating photo carriers.

Theoretical investigation of the ground state energy levels of the frontier molecular orbitals of the hydrogen bonded dimer geometry of the co-crystal reveals that in the self-assembled co-crystal TBTA acts as donor whereas QUIN acts as acceptor when they interact through hydrogen bonding interactions. The Mulliken charge distribution analysis of the hydrogen bonded dimer (Table S11†) clearly indicates that an appreciable amount of charge has been transferred from donor TBTA to acceptor QUIN. Moreover, the MEP analysis has revealed that in the co-crystal the aromatic ring of the QUIN molecule is electron rich (π -e) while the aromatic ring

of TBTA is positively charged and acts as an electron deficient π -hole (π -h) (Fig. S24†). Thus, in the solid state, holes are created in the VB and the co-crystal acts as a p-type semiconductor as the concentration of holes in the VB is greater than the concentration of electrons in the CB. It may therefore be concluded that the π – π and hydrogen bonding interactions together play the key role in assembling the co-crystal and introducing the semiconducting behaviour in it. The weak intermolecular π – π , Br \cdots π and Br \cdots O interactions provide the pathway for electrical conduction.

Optoelectronic behaviour of a material can be understood by correlating the results of optical property analysis and the study of the electrical transport properties under light illumination. The absorption coefficient *versus* photon energy plot indicates the wavelengths prone to photon absorption whereas the optical conductivity *versus* photon energy plot provides the information regarding the change in conductivity due to photon absorption. From the theoretical calculations it has been found that when the co-crystal is exposed to a photon beam, the real part of the complex conductivity exhibits a peak at 3.06 eV and an absorption peak has been observed at 3.10 eV. Further the optical bandgap of the co-crystal is 3.17 eV and the calculated electronic bandgap is 2.835 eV. All these results together indicate that when the co-crystal is exposed to visible light it absorbs photons with energy \sim 3 eV (the blue-violet region of visible light) and its conductivity increases in consequence of the photon absorption. It may be inferred that the bandgap energy is appropriate for transferring the electrons from the valence band to conduction band by absorbing the photons in the blue-violet region of the visible beam of light. Thus, holes are generated in the valence band and electron concentration in the conduction band increases. Therefore while performing the *I*–*V* measurements under visible light illumination, carriers have been generated due to the photo-responsive behaviour of the co-crystal. This leads to an increase in carrier concentration and subsequently the conductivity of the sample. Further NTO analysis reveals the presence of excitons in the sample. Thus there is another possibility that under visible light illumination the excitons in the co-crystal absorb energy from the incident photon beam and it breaks into electrons and holes and as a result the carrier concentration increases.

Conclusion

We have thoroughly examined the crystal structure, supramolecular structure, noncovalent interactions, band structure, optical properties, electronic transport mechanism and photo-responsive behaviour of a donor–acceptor co-crystal assembled by mainly π – π stacking and hydrogen bonding interactions along with minute contribution from halogen interactions. In conclusion, it has been shown that (i) apart from CT interaction, π – π and hydrogen bonding interactions can play a crucial role in formation of D–A type co-crystals, (ii) the co-crystal emits blue light under UV irradiation, (iii) a device fabricated with the co-crystal

exhibits Schottky barrier diode behaviour and photo-responsive properties, (iv) the conductivity, mobility and carrier concentration of the co-crystal increase significantly upon visible light illumination, (v) π – π and hydrogen bonding interactions together can incorporate semiconducting behaviour, (vi) weak intermolecular π – π , Br \cdots π and Br \cdots O interactions provide the pathway for electrical conduction and (vii) in this sample carriers have been generated by transfer of electrons from the valence band to the conduction band or formation of electron/hole pairs by disintegration of excitons upon photon absorption.

Conflicts of interest

The authors declare no competing financial interest.

Acknowledgements

SS gratefully acknowledges DST, Govt. of India for providing a fellowship under the DST INSPIRE program. The PURSE and FIST programs of DST, Govt. of India are also acknowledged. Financial support from the UGC, New Delhi, DST, Govt. of India, through DRS (SAP-I) and FIST programs to Department of Physics, Jadavpur University are also acknowledged. RS also acknowledges SERB, Government of India for SERB-TARE project (File No: TAR/2018/000744).

References

- 1 C. Wang, H. Dong, L. Jiang and W. Hu, *Chem. Soc. Rev.*, 2018, **47**, 422–500.
- 2 D. Yang and D. Ma, *Adv. Opt. Mater.*, 2019, **7**, 1800522.
- 3 E. Orgiu, N. Crivillers, M. Herder, L. Grubert, M. Patzel, J. Frisch, E. Pavlica, D. C. Duong, G. Bratina, A. Salleo, N. Koch, S. Hecht and P. Samori, *Nat. Chem.*, 2012, **4**, 675–679.
- 4 M. Chaudhry, K. Muhieddine, R. Wawrzinek, J. Li, S. Lo and E. Namdas, *ACS Photonics*, 2018, **5**, 2137–2144.
- 5 Y. Yamamoto, G. Zhang, W. Jin, T. Fukushima, N. Ishii, A. Saeki, S. Seki, S. Tagawa, T. Minari, K. Tsukagoshi and T. Aida, *Proc. Natl. Acad. Sci. U. S. A.*, 2009, **106**, 21051–21056.
- 6 G. R. Desiraju, *Crystallogr. Rev.*, 2020, **26**, 64–65.
- 7 R. Thakuria, N. K. Nath and B. K. Saha, *Cryst. Growth Des.*, 2019, **19**, 523–528.
- 8 Y. Liu, Q. Zeng, B. Zou, Y. Liu, B. Xu and W. Tian, *Angew. Chem., Int. Ed.*, 2018, **57**, 15670–15674.
- 9 X. D. Wang, Z. Z. Li, M. P. Zhuo, Y. Wu, S. Chen, J. N. Yao and H. B. Fu, *Adv. Funct. Mater.*, 2017, **27**, 1703470.
- 10 M. Zhuo, Y. Tao, X. Wang, Y. Wu, S. Chen, L. Liao and L. Jiang, *Angew. Chem.*, 2018, **130**, 11470–11474.
- 11 S. J. Kang, S. Ahn, J. B. Kim, C. Schenck, A. M. Hiszpanski, S. Oh, T. Schiros, Y. Loo and C. Nuckolls, *J. Am. Chem. Soc.*, 2013, **135**, 2207–2212.
- 12 A. Mandal, A. Choudhury, P. K. Iyer and P. Mal, *J. Phys. Chem. C*, 2019, **123**, 18198–18206.
- 13 N. Yee, A. Dadvand and D. F. Perepichka, *Mater. Chem. Front.*, 2020, **4**, 3669–3677.

- 14 K. K. Ray, G. Campillo-Alvarado, H. Morales-Rojas, H. Höpfl, L. R. MacGillivray and A. V. Tivanski, *Cryst. Growth Des.*, 2020, **20**, 3–8.
- 15 S. Singha, S. Goswami, S. K. Dey, R. Jana, P. P. Ray, I. Saha, C. Rizzoli, P. Bag, S. Kumar and R. Saha, *CrystEngComm*, 2020, **22**, 8197–8207.
- 16 Z. Wang, F. Yu, J. Xie, J. Zhao, Y. Zou, Z. Wang and Q. Zhang, *Chem. – Eur. J.*, 2020, **26**, 3578–3585.
- 17 S. K. Park, J. H. Kim, T. Ohto, R. Yamada, A. O. F. Jones, D. R. Whang, I. Cho, S. Oh, S. H. Hong, J. E. Kwon, J. H. Kim, Y. Olivier, R. Fischer, R. Resel, J. Gierschner, H. Tada and S. Y. Park, *Adv. Mater.*, 2017, **29**, 1701346.
- 18 F. Cicoira and C. Santato, *Adv. Funct. Mater.*, 2007, **17**, 3421.
- 19 D. Liu, J. De, H. Gao, S. Ma, Q. Ou, S. Li, Z. Qin, H. Dong, Q. Liao, B. Xu, Q. Peng, Z. Shuai, W. Tian, H. Fu, X. Zhang, Y. Zhen and W. Hu, *J. Am. Chem. Soc.*, 2020, **142**, 6332–6339.
- 20 X. D. Wang, Z. Z. Li, M. P. Zhuo, Y. Wu, S. Chen, J. N. Yao and H. B. Fu, *Adv. Funct. Mater.*, 2017, **27**, 1703470.
- 21 W. Yu, X. Wang, J. Li, Z. Li, Y. Yan, W. Wang and J. Pei, *Chem. Commun.*, 2013, **49**, 54–56.
- 22 C.-H. Liu, M. R. Niazi and D. F. Perepichka, *Am. Ethnol.*, 2019, **131**, 2–11.
- 23 H. Zhang, L. Jiang, Y. Zhen, J. Zhang, G. Han, X. Zhang, X. Fu, Y. Yi, W. Xu, H. Dong, W. Chen, W. Hu and D. Zhu, *Adv. Electron. Mater.*, 2016, **2**, 1500423.
- 24 J. Tsutsumi, T. Yamada, H. Matsui, S. Haas and T. Hasegawa, *Phys. Rev. Lett.*, 2010, **105**, 226601.
- 25 G. Griffini, L. Brambilla, M. Levi, C. Castiglioni, M. Del Zoppo and S. Turri, *RSC Adv.*, 2014, **4**, 9893–9897.
- 26 T. Goh, J.-S. Huang, K. G. Yager, M. Y. Sfeir, C.-Y. Nam, X. Tong, L. M. Guard, P. R. Melvin, F. Antonio, B. G. Bartolome, M. L. Lee, N. Hazari and A. D. Taylor, *Adv. Energy Mater.*, 2016, **6**, 1600660.
- 27 S. J. Kang, S. Ahn, J. B. Kim, C. Schenck, A. M. Hiszpanski, S. Oh, T. Schiros, Y. Loo and C. Nuckolls, *J. Am. Chem. Soc.*, 2013, **135**, 2207.
- 28 L. Sun, W. Zhu, F. Yang, B. Li, X. Ren, X. Zhang and W. Hu, *Phys. Chem. Chem. Phys.*, 2018, **20**, 6009–6023.
- 29 W. Zhu, X. Zhang and W. Hu, *Sci. Bull.*, 2021, **66**, 512–520.
- 30 W. Zhu, Y. Yi, Y. Zhen and W. Hu, *Small*, 2015, **11**, 2150–2156.
- 31 W. Zhu, R. Zheng, X. Fu, H. Fu, Q. Shi, Y. Zhen, H. Dong and W. Hu, *Angew. Chem., Int. Ed.*, 2015, **54**, 6785–6789.
- 32 W. Zhu, L. Zhu, Y. Zou, Y. Wu, Y. Zhen, H. Dong, H. Fu, Z. Wei, Q. Shi and W. Hu, *Adv. Mater.*, 2016, **28**, 5954–5962.
- 33 T. Wakahara, K. Nagaoka, A. Nakagawa, C. Hirata, Y. Matsushita, K. Miyazawa, O. Ito, Y. Wada, M. Takagi, T. Ishimoto, M. Tachikawa and K. Tsukagoshi, *ACS Appl. Mater. Interfaces*, 2020, **12**(2), 2878–2883.
- 34 X.-G. Yang, Z.-M. Zhai, X.-M. Lu, L.-F. Ma and D. Yan, *ACS Cent. Sci.*, 2020, **6**, 1169–1178.
- 35 W. Yu, X. Wang, J. Li, Z. Li, Y. Yan, W. Wang and J. Pei, *Chem. Commun.*, 2013, **49**, 54.
- 36 S. K. Dey, R. Saha, S. Biswas, A. Layek, S. Middy, I. M. Steele, M. Fleck, P. P. Ray and S. Kumar, *Cryst. Growth Des.*, 2014, **14**, 207–221.
- 37 S. K. Cheung and N. W. Cheung, *Appl. Phys. Lett.*, 1986, **49**, 85–87.
- 38 N. F. Mott and R. W. Gurney, *Electronic Processes in Ionic Crystals*, Clarendon Press, Oxford, 1940.
- 39 J. A. Röhr, D. Moia, S. A. Haque, T. Kirchartz and J. Nelson, *J. Phys.: Condens. Matter*, 2018, **30**, 105901.
- 40 A. Dey, A. Layek, A. Roychowdhury, M. Das, J. Datta, S. Middy, D. Das and P. P. Ray, *RSC Adv.*, 2015, **5**, 36560–36567.
- 41 R. K. Gupta and F. Yakuphanoglu, *Sol. Energy*, 2012, **86**, 1539–1545.
- 42 M. Das, J. Datta, A. Dey, R. Jana, A. Layek, S. Middy and P. P. Ray, *RSC Adv.*, 2015, **5**, 101582–101592.
- 43 R. Jana, A. Dey, M. Das, J. Datta, P. Das and P. P. Ray, *Appl. Surf. Sci.*, 2018, **452**, 155–164.